scientific reports

Check for updates

OPEN

Towards Room Temperature Thermochromic Coatings with controllable NIR-IR modulation for solar heat management & smart windows applications

B. S. Khanyile[1,2✉], N. Numan[1,2], A. Simo[1,2], M. Nkosi[1,2], C. B. Mtshali[1], Z. Khumalo[1], I. G. Madiba[1,2], B. Mabakachaba[1,2,3], H. Swart[4], E. Coetsee-Hugo[4], Mart-Mari Duvenhage[4], E. Lee[4], M. Henini[5], A. Gibaud[6], M. Chaker[7], P. Rezaee[1,2], N. Lethole[8], M. Akbari[1,2], R. Morad[1,2] & M. Maaza[1,2✉]

Solar heat management & green air-conditioning are among the major technologies that could mitigate heat islands phenomenon while minimizing significantly the CO_2 global foot-print within the building & automotive sectors. Chromogenic materials in general, and thermochromic smart coatings especially are promising candidates that consent a noteworthy dynamic solar radiation Infrared (NIR-IR) regulation and hence an efficient solar heat management especially with the expected increase of the global seasonal temperature. Within this contribution, two major challenging bottlenecks in vanadium oxide based smart coatings were addressed. It is validated for the first time that the NIR-IR modulation of the optical transmission ($\Delta T_{TRANS} = T_{(T\langle TMIT)} - T_{(T\rangle TMIT}$) of Vanadium oxide based smart coatings can be controlled & tuned. This upmost challenging bottle-neck controllability/ tunability is confirmed via a genuine approach alongside to a simultaneous drastic reduction of the phase transition temperature T_{MIT} from 68.8 °C to nearly room temperature. More precisely, a substantial thermochromism in multilayered $V_2O_5/V/V_2O_5$ stacks equivalent to that of standard pure VO_2 thin films but with a far lower transition temperature, is reported. Such a multilayered $V_2O_5/V/V_2O_5$ thermochromic system exhibited a net control & tunability of the optical transmission modulation in the NIR-IR (ΔT_{TRANS}) via the nano-scaled thickness' control of the intermediate Vanadium layer. In addition, the control of ΔT_{TRANS} is accompanied by a tremendous diminution of the thermochromic transition temperature from the elevated bulk value of 68.8 °C to the range of 27.5–37.5 °C. The observed remarkable and reversible thermochromism in such multilayered nano-scaled system of $V_2O_5/V/V_2O_5$ is likely to be ascribed to a noteworthy interfacial diffusion, and an indirect doping by alkaline ions diffusing from the borosilicate substrate. It is hoped that the current findings would contribute in advancing thermochromic smart window technology and their applications

[1]MRD-Tandetron Accelerator & Nanosciences African Network, iThemba LABS-National Research Foundation, P O Box 722, Somerset West 7129, Western Cape Province, South Africa. [2]UNESCO-UNISA Africa Chair in Nanosciences and Nanotechnology, College of Graduate Studies, University of South Africa, Muckleneuk Ridge, P.O. Box 392, Pretoria 003, South Africa. [3]Physics Department, University of the Western Cape, P.O. Box 1906, Bellville 7535, South Africa. [4]Faculty of Natural and Agricultural Sciences, Physics Department, University of the Free State, P.O. Box 339, Bloemfontein 9300, Republic of South Africa. [5]School of Physics & Astronomy, Nottingham University, Nottingham NG7 2RD7, UK. [6]IMMM, UMR 6283 CNRS, Bd O. Messiaen, University of Le Maine, 72085 Le Mans Cedex 09, France. [7]INRS-Energie et Matériaux, 1650 Lionel-Boulet, Varennes, Québec J3X 1S2, Canada. [8]Department Physics, University of Fort Hare, Alice, Eastern Cape Province, South Africa. ✉email: sfundob@gmail.com; Maazam@unisa.ac.za

for solar heat management in glass windows in general, skyscraper especially & in the automotive industry. If so, this would open a path to a sustainable green air-conditioning with zero-energy input.

The rise of the global average temperature correlated to climate change has generalized heat islands phenomenon. This latter is becoming a major concern especially with the fast rising rural to urban population exodus. Yet, this singularity was well known for almost a century, it became dominant recently as observed in densely populated cities where excessive temperatures were registered. Such recent elevated & localized temperatures are caused by the important release of anthropogenic heat, and the excess storage of solar radiation within the city compounds. In addition, it is exacerbated by the shortage of green spaces and cool sinks, the lack of effective circulation of air within the city landscape as well as the reduced ability of the emitted infrared radiations to escape in the atmosphere[1]. As summarized by Santamouris et al., Papanikolaou et al.[2–6], several potential technologies can be used to mitigate such a heat islands phenomenon. Among which; (1) Roof greening, (2) White reflective roofing, (3) Walls greening, (4) Usage of natural heat sinks view of dissipating heat excess, (5) Expanding green spaces, (6) Usage of advanced reflective materials based on nanotechnology additives such as thermochromic paints and coated glass windows[7–9], and (7) Generalization of the usage of smart windows in both buildings & automotives. This later mitigating cooling technology would not only improve the indoor thermal comfort but minimize the energy consumption due to air–conditioning in addition to the reduction of the CO_2 footprint.

As per today, ~ 55% of the world's population lives in urban areas. It is projected that it would reach ~ 2.5 billion by 2050, with ~ 90% of this increase in Asia & Africa. With such an upsurge of the urban population and climate change increase of the average seasonal atmospheric temperature, air-conditioning demand is expected to sky-rocket. The global stock of air conditioners in buildings & automotive sectors is expected to grow up to ~ 5.6 billion by 2050 from the current pool of ~ 1.6 billion today units. The International Energy Agency (IEA)'s projections[10] for the global energy demand in air-conditioning is expected to triple by 2050. This paramount increase will entail the usage of a significant electricity supply. Henceforth, sustainable technologies are required to minimize the corresponding energy pressure and the related CO_2 footprint. Chromogenics and/or radiative cooling coatings are potential genuine solutions as a sustainable pathway for green air-conditioning[11–13].

Among the chromogenic technologies, including electrochromism, and gasochromism, thermochromic nano-coatings for smart windows applications (Fig. 1) have attracted a special interest since the observation of the reversible semiconductor-metallic 1st order transition in Vanadium dioxide (VO_2) by Morin in 1959[14]. Since then, several oxides were found to exhibit such a 1st order phase transition as displayed in (Fig. 2a)[15–17]. As one can notice, several of these oxides are Vanadium based. Figure 2b reports the corresponding Pressure-Concentration stability phase- diagram of such a rich family of Vanadium oxides correlated to the multivalence of Vanadium; namely V^{+5}, V^{+4}, V^{+3}, V^{+2}, V^{+1}. Moreover, there are 2 additional large V_xO_y families including the Magnussen (V_nO_{2n+1}) & Wadsley ($V_{2n}O_{5n-2}$) layered compounds[15–18]. However, VO_2 was and is the most investigated compound in view of its sharp 1st order ultrafast phase transition taking place at the vicinity of $T_{MIT} \sim 68\ °C$[14,18,19]
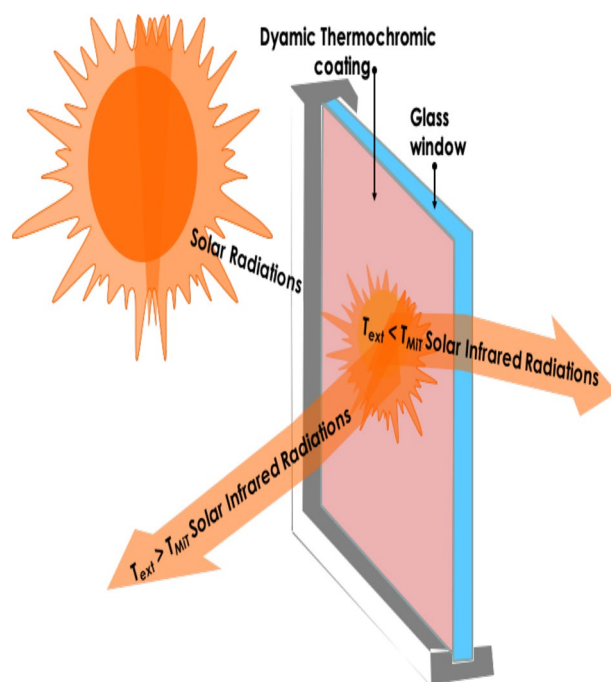

Figure 1. Dynamic solar heat management in VO_x based smat window. &Schematic representation of a thermochromic coated glass window,
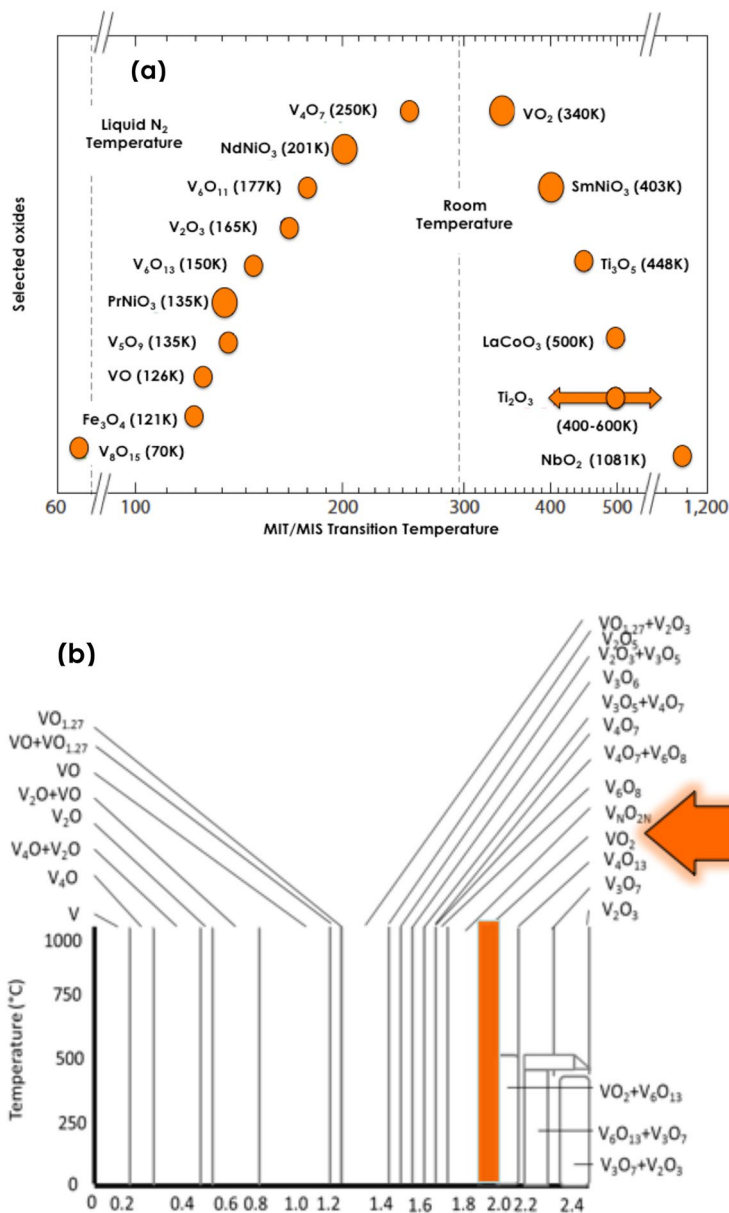
Figure 2. (**a**) Major oxides exhibiting Metallic-Insulator or Metallic-Semiconductor phase transition [Dominated by Vanadium oxides]. (**b**) Temperature-Oxygen Concentration phase diagram of the V–O system.

which is close to room temperature and hence the corresponding potential technological applications in solar heat management as intelligent coating for smart windows in the building and automotive sectors in particular[11].

Indeed, and as demonstrated both experimentally and theoretically, VO_2 exhibits a 1st order reversible phase transition from a semiconductor state to a metallic state & vis-versa upon heating/cooling[11–14]. Such a reversible phase transition which can be stimulated via an external thermal, pressure or optical stimuli is both crystal-lographic and electronic[18,19]. From crystallographic viewpoint, the low temperature monoclinic VO_2 structure transits reversibly to a tetragonal phase above $T_{MIT} \sim 68$ °C (Fig. 3a). Such a femtosecond crystallographic transition is correlated to an electronic transition. This later originates from the splitting of the d// band inducing the creation of a band-gap of the order of 0.72 eV below $T_{MIT} \sim 68$ °C which closes above (Fig. 3b)[15].

Besides the thermochromic properties for smart windows applications, VO_2 was found to be effective in a variety of technological applications. This includes o tunable nano-plasmonics[20,21], ultrafast optoelectronic gating[22,23], chemresistors for H_2 gas sensing[24,25] and tunable emissivity space coatings for small satellites[26,27] as well as optical limiting and laser radiations protection coatings[28–30].

In addition to these multifunctionalities, VO_2 & related family oxides have raised and impacted substantially several fundamental questions in condensed matter specifically & solid state physics in general. As reported in Table 1, this includes but not limited to: shed-lighting on the sliding twin-domains in self-heated needle-like VO_2 single crystals[31], evolution of the Mott transition in chain structure of strained VO_2 films revealed by coherent
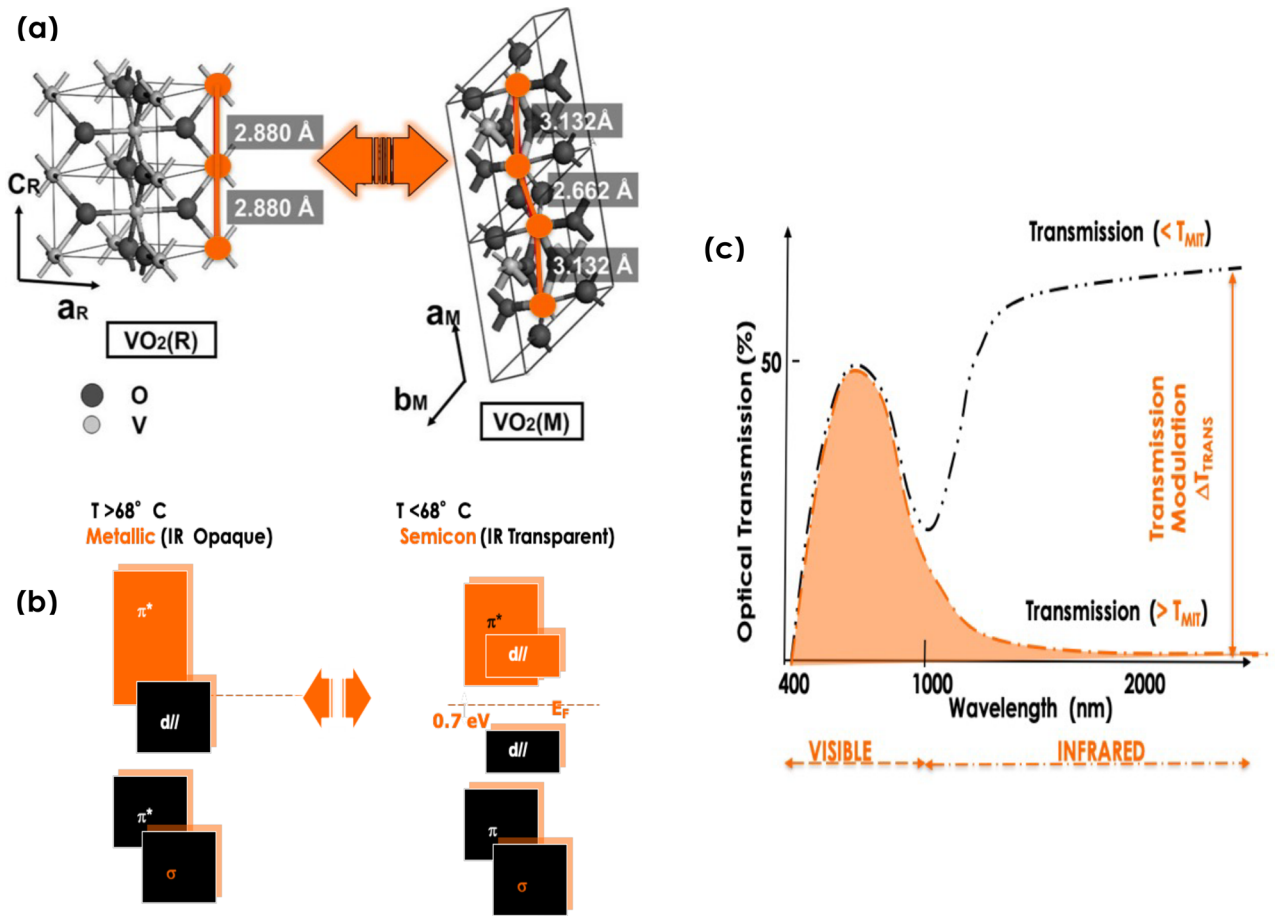
Figure 3. Major properties related to the VO$_2$ 1st order phase transition. (**a**) Reversible Monoclinic-Rutile crystallographic phase transition of VO$_2$ at the vicinity of T$_{MiT}$ ~ 68 ºC, (**b**) The corresponding reversible electronic phase transition due to the reversible opening-closing of the d band orbital, (**c**) Ideal optical response of a VO$_2$ based thermochromic coating; (1) T$_{VIS}$ > 50%), (2) T$_{MIT}$ ~ 25 °C) and primarily, a large modulation in the (NIR) & (IR) spectral range (ΔT$_{TRANS}$).

phonons[32], investigation of the solid-state triple point at the metal–insulator transition in VO$_2$[33], Observation of a large non-thermal contribution to picosecond strain pulse generation using the photo-induced phase transition in VO$_2$[34], elucidating on the inhomogeneity of the ultrafast insulator-to-metal transition dynamics of VO$_2$[35], clarifying the transient dynamics of the phase transition in VO$_2$ revealed by mega-electron-volt ultrafast electron diffraction[36], observation of the magnetic-field-induced insulator–metal transition in W-doped VO$_2$ at 500 T[37], demonstration of the reversible phase modulation and hydrogen storage in multivalent VO$_2$ epitaxial thin films[38], Decoupling the Lattice Distortion and Charge Doping Effects on the Phase Transition Behavior of VO$_2$ by Titanium (Ti^{4+}) Doping[39], Observation of the photo-induced non-volatile VO$_2$ phase transition for neuromorphic ultraviolet sensors[40] in addition to numerous ultrafast technological proofs of concept[41–43].

Yet, the above mentioned technological applications and fundamental focii are directly related to the modulation of the optical transmission of the VO$_2$ in the NIR-IR spectral region especially, this latter is the pivotal and central parameter for solar heat management & smart windows applications[10–12,16,17]. As schematically summarized in Fig. 3c, an ideal VO$_2$ based thermochromic coating should exhibit the following major characteristics: (1) a good and temperature independent optical transmission in the visible (VIS) spectral range (with a priori a VIS transmission > 50%), (2) a phase transition temperature T$_{MIT}$ close to room temperature (far below the bulk VO$_2$ transition of T$_{MiT}$ ~ 68 °C) and primarily, a noteworthy large modulation in the Near Infrared (NIR) and Infrared (IR) spectral range (ΔT$_{TRANS}$). This latter is the difference between the optical transmissions below and above T$_{MiT}$; (ΔT$_{TRANS}$ = T$_{(T\langle TMIT)}$ − T$_{(T\rangle TMIT}$ > 50%). Although, this later modulation in the NIR & IR spectral range is exceedingly challenging, the lowering of the T$_{MIT}$ and the raising of the VIS optical transmission have been successfully dealt with through an adequate doping (W, Mo, Mg,…) and via the usage of an additional anti-reflection treatment (TiO$_2$, ZrO$_2$,ZnO,…) respectively[44–48].

In the pursuit of engineering optimal thermochromic VO$_2$ based coatings with a substantial elevated and tunable modulation in the NIR-IR spectral range (ΔT$_{TRANS}$ = T$_{(T\langle TMIT)}$ − T$_{(T\rangle TMIT}$), several physical & chemical methodologies were & are used for its deposition[49–61]. Excluding limited cases, the general usage of single and unique layer of VO$_2$ was and is the dominating trend in thermochromic VO$_2$ based applications. Likewise, in its doped or un-doped form, the VO$_2$ based thermochromic coatings suffer in terms of modulation in the Infrared

System's Configuration	Investigated major phenomena & properties	References
VO$_2$ Single crystal	Sliding twin-domains in self-heated needle-like VO$_2$ single crystals	[31]
VO$_2$ Strained thin films	Mott transition in chain structure of strained VO$_2$ films revealed by coherent phonons	[32]
Single-crystal VO$_2$ nanobeams	Measurement of a solid-state triple point at the metal–insulator transition in VO$_2$	[33]
VO$_2$ Single crystal	Observation of a large non-thermal contribution to picosecond train pulse generation using the photo-induced phase transition in VO$_2$	[34]
VO$_2$ Single crystal	Elucidating the inhomogeneity of the ultrafast insulator-to-metal transition dynamics of VO$_2$	[35]
VO$_2$ Single crystal	Clarification of the transient dynamics of the phase transition in VO$_2$ revealed by mega-electron-volt ultrafast electron diffraction	[36]
W-doped VO$_2$ thin films	observation of the magnetic-field-induced insulator–metal transition in W-doped VO$_2$ at 500 T	[37]
VO$_2$ epitaxial thin films	demonstration of the reversible phase modulation & hydrogen storage in multivalent VO$_2$ epitaxial thin films	[38]
Ti$_x$V$_{1-x}$O$_2$ nanopowders	Decoupling the Lattice Distortion and Charge Doping Effects on the Phase Transition Behavior of VO^2 by Titanium (Ti^{4+}) Doping	[39]
VO$_2$ Thin films	Photo-induction in non-volatile VO$_2$ phase transition for neuromorphic ultraviolet sensors	[40]
VO$_2$ ultrathin films on Si$_3$N$_4$ membranes	Ultrafast X-ray imaging of the light-induced phase transition in VO$_2$	[41]
VO$_2$ Single crystal	Demonstration of the reversible switching between pressure induced amorphization and thermal-driven recrystallization in VO$_2$(B) nanosheets	[42]
ultrathin VO$_2$ channels	Validation of the positive-bias gate-controlled metal–insulator transition in ultrathin VO2 channels with TiO2 gate dielectrics	[43]

Table 1. Selected recent major findings in VO$_2$ based systems.

region (ΔT_{TRANS}). The same situation is faced even in the case of the VO$_2$ deposition onto various substrates; amorphous (glass, PET,…)[44,45] or crystalline (Quartz, Silicon, Mica,…)[46–48,62–73] in nature. Simply summarized, the VO$_2$ based thermochromic coatings suffer drastically in terms of modulation in the Infrared region (ΔT_{TRANS}) specifically.

In this regard, and within the novelty & originality of this contribution, it is validated for the first time that the NIR-IR modulation of the optical transmission (ΔT_{TRANS}) can be controlled/tuned via an authentic novel approach with a simultaneous drastic reduction of T_{MIT}. This latter original approach consists of using a multi-layered configuration instead of the standard single VO$_2$ layer approach as illustrated in Fig. 4a. In addition, it requires the usage of a Magnussen V oxide such as V$_2$O$_5$ and not the standard pure VO$_2$. For the validation of such a NIR-IR modulation control with a simultaneous drastic reduction of T_{MIT}, a tri-layer stack consisting of V$_2$O$_5$/V/V$_2$O$_5$ deposited onto glass substrate was considered. Within such a multi-layered stack of V$_2$O$_5$/V/V$_2$O$_5$ onto borosilicate glass substrate, the V$_2$O$_5$ layers' thickness is fixed and that of the interlayer of pure V is varied followed by an optimal post annealing.

Yet original in terms of approach, it is to be stressed that this research work has been inspired by several partial contributions including but not limited to Long et al.[74], Pellegrino et al.[75], Wang, Miller et al.[76], Zheng et al.[77], Zhou et al.[78], Han et al.[79], Zhao et al.[80] while fostering the previous work by Sfundo et al.[81]. As per the scientific & patented published literature, and as it was highlighted previously, other multi-layered nano-structures were proposed but none allowed a significant control of the NIR-IR modulation with a significant decrease of the T_{MIT} simultaneously. Table 2 summarizes such multilayered nano-structures.

The specific objectives of this contribution are as follows.

1. Validation of thermochromism in V$_2$O$_5$/V/V$_2$O$_5$ sandwich nanostructures,
2. Validation of the tunability/control of the modulation in the NIR-IR spectral range ($\Delta T_{TRANS} = T(T_{\langle TMIT \rangle}) - T_{(T)\rangle TMIT}$),
3. Validation of the tunability/control of the transition temperature T_{MIT},
4. Validation of the effectiveness of Alkaline doping in T_{MIT} tenability.

Comparatively to the previous published literature as recapitulated in Table 2, the current research contributes in advancing the subject of Vanadium oxide based thermochromism via two major milestones; (1) the crucial role of the intermediate V layer within the V$_2$O$_5$/V/V$_2$O$_5$ sandwich nanostructures in terms of the tunability of both the optical modulation in the NIR-IR spectral range ($\Delta T_{TRANS} = T(T_{\langle TMIT \rangle}) - T(T)_{\rangle TMIT}$), and that of the transition temperature T_{MIT}, (2) the role of the alkaline ions doping originating from the borosilicate substrate. As per our best knowledge, none of the above mentioned parameters were investigated so far.

Materials and methods
Samples preparation
All chemicals & substrates used in these experiments are of high chemical grade (from Sigma-Aldrich &/or Alfa-Aesar). Following a sequential procedure, multi-layered films of V$_2$O$_5$/V/V$_2$O$_5$ were deposited by e-beam evaporation using V$_2$O$_5$ powder and V metal material targets and borosilicate glass substrates ($10 \times 10 \times 2.5$ mm^3). The substrates were cleaned in an ultrasonic bath with methanol and de-ionized water for ~ 20 min prior to
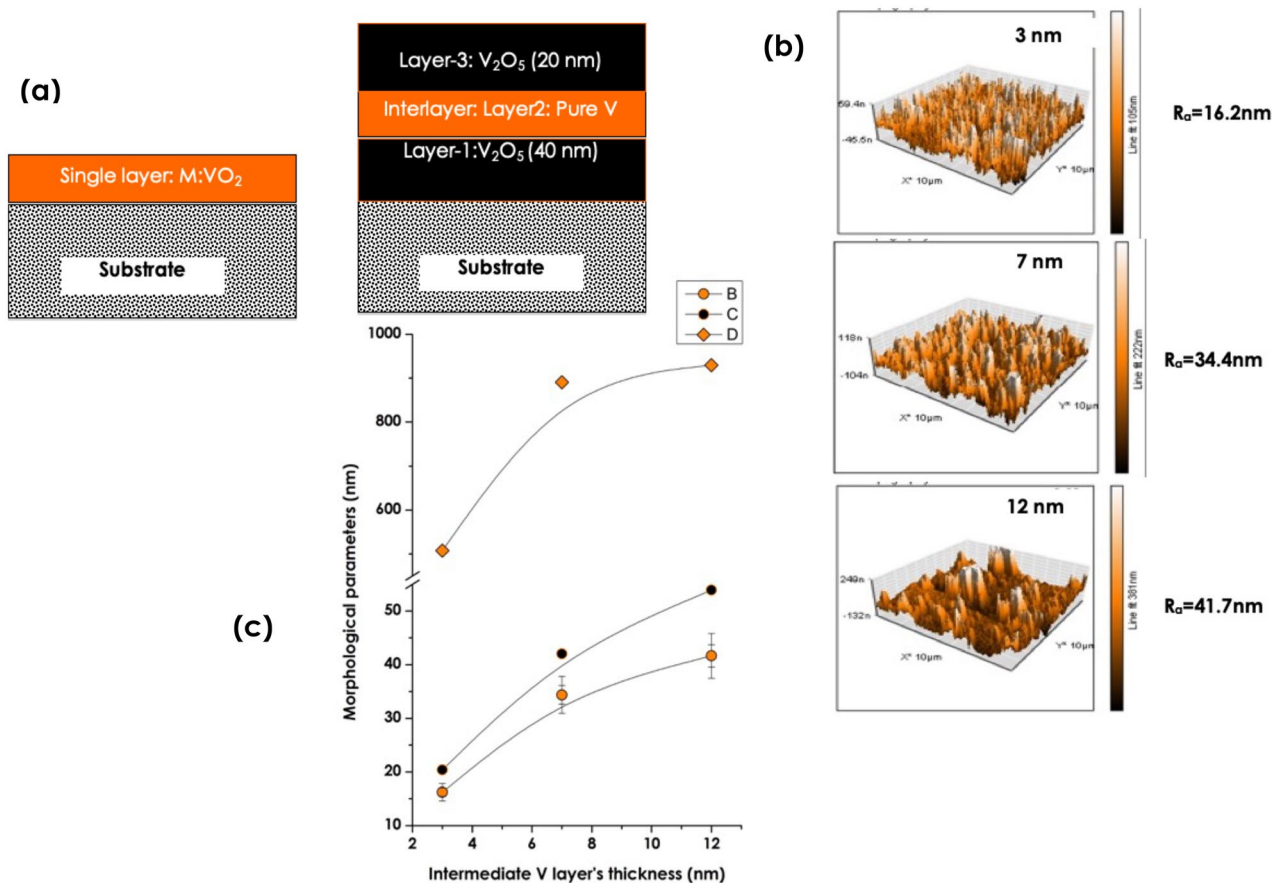
Figure 4. Configurations of the engineered thermochromic coating & its major surface morphological characteristics. (**a**) Standard Single VO_2 layer configuration & the current considered multi-layered structure consisting of V_2O_5(Fixed thickness:20 nm)/pure V (Variable thickness)/V_2O_5 (Fixed thickness:40 nm) deposited onto glass substrate, (**b**) Surface Atomic Force Microscopy surface morphology of the 3 multilayered samples, (**c**) Evolution of corresponding average roughness R_a (yellow filled circles), the root mean square (R_q) (black filled circles), and the average crystallites size (Ø) (yellow filled diamonds).

Configuration of the multilayered system	Synthesis technique	Transition temperature (°C)	References
V_2O_3/VO_2	Reactive magnetron sputtering	72.0	Long et al.[74]
VO_2/TiO_2	Pulsed Laser Deposition	63.5	Pellegrino et al.[75]
ITO/VO_2/TiO_2	Reactive magnetron Sputtering	52.0	Miller and Wang[76]
TiO_2/VO_2/TiO_2	Medium frequency reactive magnetron sputtering	61.5	Zheng et al.[77]
SiO_2/VO_2	Spin coating	61.0	Wang et al.[82]
V_2O_3/V (7 nm)/V_2O_3	Electron beam Evaporation With a non optimised annealing	27.9	Sfundo et al.[81]
V_2O_3/V(12 nm)/V_2O_3	Electron beam Evaporation With a non optimised annealing	36.9	Sfundo et al.[81]
VO_2/Au/VO_2	Electron beam evaporation	66.9	Zhou et al.[78]
V_2O_5/V/V_2O_5	Electron beam evaporation	high-temperature coefficient of resistance	Han et al.[79]
SiO_2-TiO_2/VO_2/ TiO_2	Spin coating	36.9	Zhao et al.[80]
WO_3/VO_2/WO_3	Reactive magnetron sputtering	54.5	Long et al.[83]
V_2O_5/V(7 nm)/V_2O_5	Electron beam evaporation	27.5	Current work
V_2O_5/V12nm)/V_2O_5	Electron beam evaporation	37.5	Current work

Table 2. Major published VO_2 based multilayered coatings.

deposition. All substrates were dried with pressurized 100% pure N_2 gas before being loaded into the deposition chamber, which was already loaded with highly pure vanadium (V) and vanadium pentoxide (V_2O_5) targets in separate crucibles. The multi-layered stacks were deposited at an initial chamber vacuum pressure of ~ 10^{-6} mbar and an evaporation rate of ~ 0.24 nm/s. The V_2O_5 & pure V layers' thicknesses were monitored with a standard crystal monitor. The thickness of the 1st layer (bottom) of V_2O_5, was fixed to ~ 40 nm, while the thickness of the intermediate layer (V layer) was varied within a defined range of 3–12 nm at specific values of 3, 7 and 12 ± 0.2 nm. The thickness of the 3rd (top layer) of (V_2O_5) was fixed at 20 nm. These thicknesses were chosen based on a preliminary set of computations, which suggested that the film be chosen in such a way that sufficient diffusion of oxygen into that inter-layer would take place in addition of an additional interfacial stress/strain; with both layers allowing O atoms to diffuse into the V intermediate layer. All prepared samples were annealed for 120 min in a vacuum of ~ 10^{-6} mbar at the temperature of 500 °C.

Samples characterization

The surface morphology of the samples was investigated using Atomic Force Microscopy (AFM) in non-contact mode complemented by an in-depth/volume morphology studies using a Field Emission Scanning Electron Microscopy (FE-SEM, Jeol JSM-7800F). The crystal structure of the various samples was examined with a Bruker AXS D8 Advanced X-ray diffractometer, which was outfitted with a copper X-ray tube (λ = 0.15406 nm) and operated at 40 kV and 40 mA with data collection in the Θ–2Θ configuration within the angular range of 15–60 Deg (in steps of 0.01 Deg). For the elemental analysis and depth profiling, Auger Electron Spectroscopy (AES) and Time of Flight Secondary Ion Mass Spectrometry (ToF-SIMS) were used. The optical measurements within the spectral range of 250–2500 nm were carried out in transmittance mode (normal incidence) with a Cary 5000 UV–VIS–NIR spectrometer equipped with a controllable heating stage with a heating/cooling rate of 5 °C/min within the temperature range of 20–90 °C.

Results and discussions

Morphological investigations: AFM & FE SEM

Figure 4b displays the Atomic Force Microscopy of the various samples. The surfaces are relatively rough suggesting, a priori, the crystalline nature of the multi-layered stack samples or at least the top surface of layer 3 (V_2O_5 top layer). Table 3 summarizes the corresponding values of the average roughness (R_a), the root mean square (R_σ), the average height (H) as well as the average crystallites size (Ø). Accordingly, thicker is the intermediate V layer, higher are the various parameters $\langle R_a \rangle$, $\langle R_\sigma \rangle$, $\langle H \rangle$ and $\langle Ø \rangle$. Yet limited to 3 values of the intermediate V layer's thickness, it can be safely concluded that the effect of this latter (i.e. the intermediate V layer's thickness) is of a prime effectiveness in view of the variations of Table 3 & Fig. 4c.

Figure 5 displays the FESEM edge cross-section of the various multi-layered samples. As one can notice, in each and all of the samples, it is not possible to distinguish the various layers of the stacks V_2O_5/V/V_2O_5 deposited onto the borosilicate glass substrates. Indeed, excluding the crystal-clear net interface with the substrate, there are no sharp interfaces between bottom layer 1 (V_2O_5) and the intermediate V layer as well as this latter and top layer 3 (V_2O_5). This is likely a signature of a noteworthy interfacial diffusion within both interfaces of the intermediate layer of V and top/bottom surrounding layers of V_2O_5. This observation seems to be supported by the observed various nano-crystals distributed isotropically within the transversal direction of the stack throughout the 2 interfaces of Fig. 5. If one considers the O and V atomic/ionic radii, it could be, safely concluded that Oxygen is prospectively to diffuse from the O rich regions i.e. from layers 1 & 3 of V_2O_5 towards the O poor region i.e. towards the pure V intermediate layer. Last but not least, one can observe several cracks within the substrate of sample 3 i.e. (12 nm V intermediate layer thickness). These cracks seem to be initiated from layer 1-substrate interface and propagating towards the inner section of the substrate. These cracks are likely to originate from a substantial stress/strain relaxation at the interface layer 1/substrate at least. As a preliminary pre-conclusion of this section, one could cautiously conclude on the elevated interfacial diffusion within the interfaces (top & bottom) surrounding the intermediate layer of pure Vanadium. Such a significant interfacial diffusion would not only affect the chemical composition profile of the multi-layered stack but also the strain/stress distribution.

Elemental analysis & depth profiling: Auger analysis

Figure 6a displays the elemental depth profiling of Carbon (C), Oxygen (O), Vanadium (V) and Silicon (Si) of the 3 samples obtained via Auger spectrometry investigations. The C originates from the Carbon coating layer deposited onto the surface sample initially for charge removal. By contrast, Si originates from the borosilicate glass substrate. This latter consists of 70–80 wt% SiO_2 of amorphous SiO_2 in addition to other oxides (7–13 wt% of B_2O_3, 4–8 wt% Na_2O, K_2O, and 2–8 wt% of Al_2O_3[84]. As one can notice, the Si diffusion is mainly localized at the substrate-1st layer of V_2O_5 in the 3 multi-layered stacks independently from the intermediate V layer's

Sample identification	Intermediate V layer thickness (nm)	Average roughness $\langle R_a \rangle$ (nm)	Root Mean Square roughness $\langle R_\sigma \rangle$ (nm)	Average height H $\langle H \rangle$ (nm)	Average Grain size $\langle Ø \rangle$ (nm)
V_2O_5/3nmV/V_2O_5	3	16.21	20.39	1.04	507.82
V_2O_5/7nmV/V_2O_5	7	34.37	42.04	2.36	890.62
V_2O_5/12nmV/V_2O_5	12	41.65	53.93	2.47	929.76

Table 3. AFM characteristic parameters of thermal annealed multi-layered films.
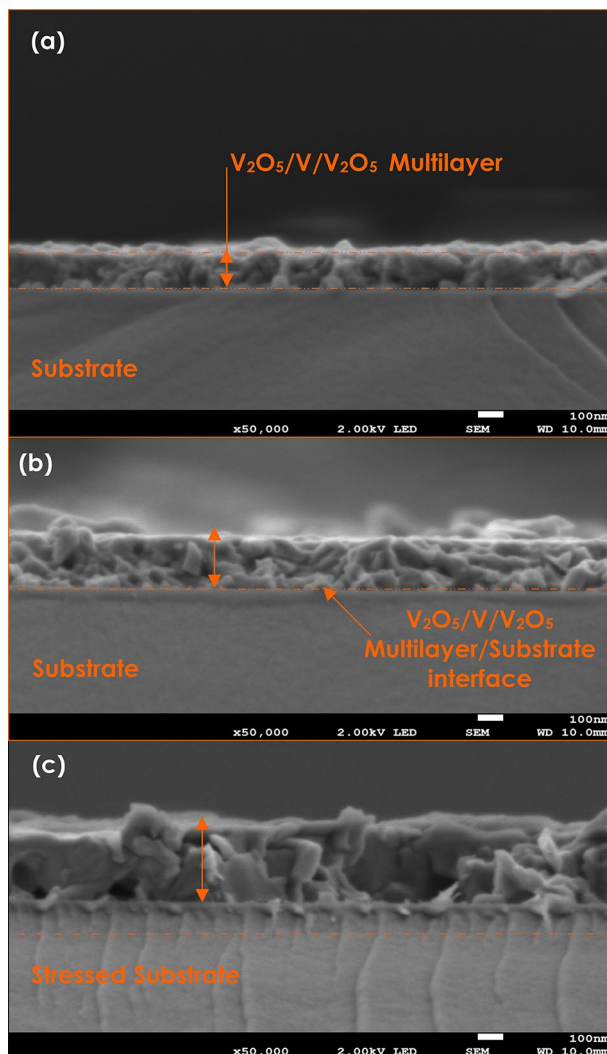
Figure 5. In volume cross-section of the various multi-layered V_2O_5 (20 nm)/pure V (Variable thickness)/V_2O_5 (40 nm) deposited onto glass substrate & their Auger elemental depth profiling.

thickness. Hence, one could, a priori, conclude that the 1st layer of V_2O_5 might acted as a barrier minimizing the diffusion of Si & Al from the borosilicate substrate towards the multi-layered stack.

By contrast, If the O & V concentration depth profiles of Fig. 6a are considered, one can crystal clearly notice the presence of oxygen through-out the transversal direction of the 3 stacks. This is in support of the significant interfacial diffusion mentioned formerly, especially the O diffusion from the surrounding V_2O_5 layers towards the intermediate V layer.

Likewise, the O & V concentration depth profiles seem substantially correlated while in phase in the case of samples 2 ($V_{Intermediate-layer} = 7$ nm) and 3 ($V_{Intermediate-layer} = 12$ nm) by opposite to sample 1 ($V_{Intermediate-layer} = 3$ nm). Figure 6b reports the corresponding depth variation of the O/V ratio. Subsequently, and within the bar error of ± 5%, the average value of the O/V ratio seems increasing quasi linearly for sample 1 ($V_{Intermediate-layer} = 3$ nm) while fluctuating between 1.5 and 2 for sample 2 ($V_{Intermediate-layer} = 7$ nm) and sample 3 ($V_{Intermediate-layer} = 12$ nm). Henceforth, it can safely be concluded that in the 2 thicker stacks, the dominating phase or phase are within the V_2O_3 & VO_2 families from stoichiometric viewpoint and/or phases under significant strain/stress (if one considers the observed cracks relaxation in the FESEM images of Fig. 5c).

Alkaline doping via *substrate-stack interfacial diffusion & depth profiling: SIMS analysis*
Because of the small ionic radius of alkaline ions and their low activation energy, It is established that they diffuse relatively fast within the substrate surface via established exchange mechanisms[84,85]. In the case of Na^+, its low activation energy Q_a & its elevated diffusion constant D_0 ($D = D_0e - Q^a$, activation energy of $Q_a = 1.36$ eV and $D_0 = 3.12 \times 10^{-4}$ m^2) fovours its diffusion both within the bulk and the surface of the glass substrate[86,87]. Hence, it is necessary to depth profile the alkaline ions. For such Secondary Ions Mass Spectrometry (SIMS) analysis were carried out.
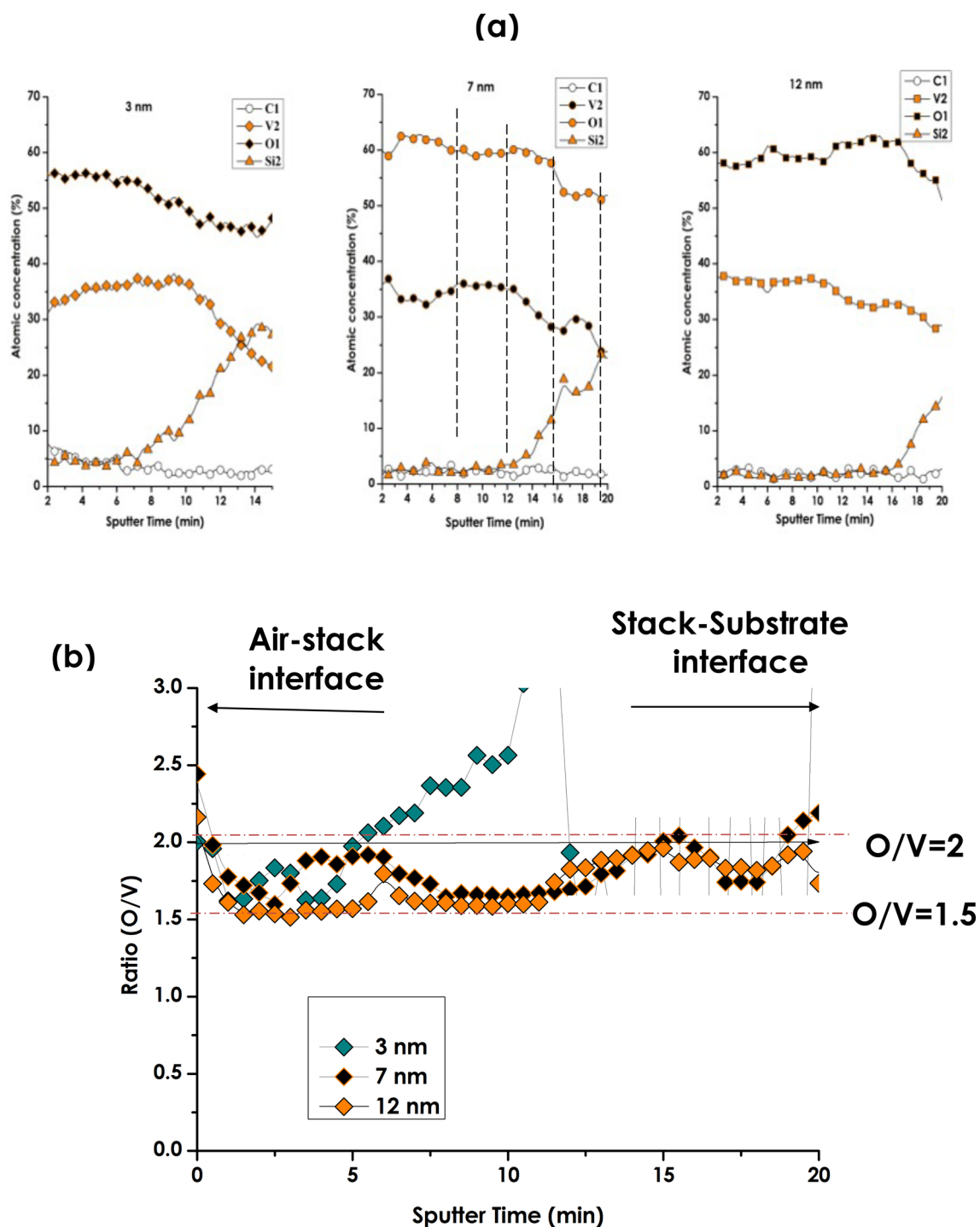
Figure 6. (**a**) The various multi-layered V_2O_5(20 nm)/pure V(Variable thickness)/V_2O_5 (40 nm)deposited onto glass substrate corresponding Auger chemical profiling of C, V, O & Si, and (**b**) the corresponding O/V ratio.

Figure 7 displays the SIMS elemental depth profiling of several ions proper to the stack (V^+, VO^+) and those alkaline ions from the borosilicate substrate (Na^+, Ca^+ & K^+). These latter explicit ions were targeted in view of the chemical composition of the borosilicate glass substrate (consisting of SiO_2: 72.5%, Na_2O: 13.7%, CaO: 9.1%, KO: 12% MgO: 4.2%,…)[70,84,86,87]. Once again, the distribution profiles of V^+, VO^+ are alike throughout the multi-layered stack samples and the stack-substrate interface. This matching depth distributions of V^+ & VO^+ is in an ample support of the O diffusion observed in the previous Auger profiles. The Si profiles exhibit a heavy-side type variation for each & all samples with a nearly zero counts within the stack in support of a very weak if not a no diffusion of Si originating from the substrate. This latter behaviour is also in accordance with the previous Auger observations. Contrasting with such a Si limited interfacial diffusion is the alkaline ions; namely Na^+, Ca^+ and K^+. All of them display a long-range diffusion from the borosilicate glass throughout the
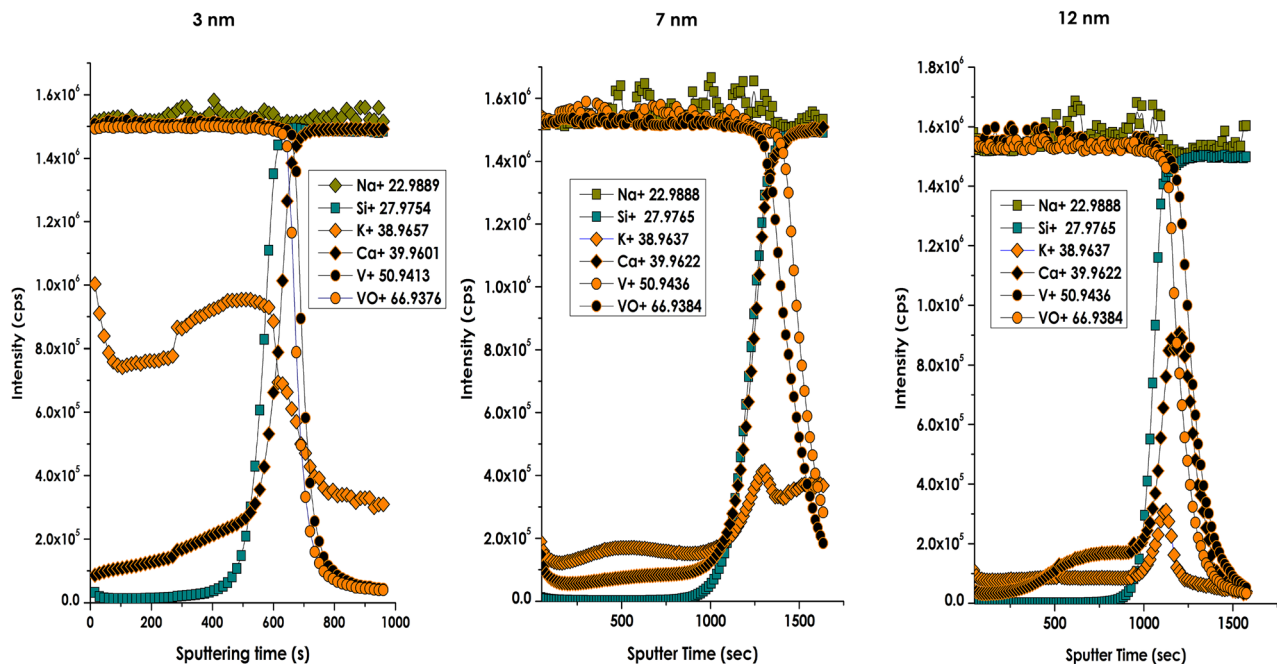
Figure 7. In-depth profile O/V ratio variation derived from Secondary Ion Mass spectrometry (SIMS) elemental depth profiling of various halides (Na$^+$, K$^+$, Ca$^+$), Silicon Si$^+$ and Vanadium (V$^+$) as well as VO$^+$ of the various multi-layered stacks of V$_2$O$_5$/V/V$_2$O$_5$ deposited onto borosilicate glass substrate for various intermediate Vanadium layer's thickness; 3 nm, 7 nm and 12 nm.

stacks with Na$^+$ followed by K$^+$ and Ca$^+$ up to the air-stacks interface. Such an prominent extended diffusion is likely due to the small ionic radius ($\varnothing_{Na+} \approx 0.102$ nm, $\varnothing_{K+} \approx 0.138$ nm, $\varnothing_{Ca+} \approx 0.118$ nm),and the low activation energy of the concerned alkaline and henceforth their elevated diffusion coefficient ($D_{oNa+} \approx 0.330 \times 10^{-9}$ m^2/s, $D_{oK+} \approx 1.960 \times 10^{-9}$ m^2/s, $D_{oCa+} \approx 0.79310^{-9}$ m^2/s) by contrast to Mg & Si as well as to V. Nevertheless, there is a crystal-clear difference between the depth distributions of Na$^+$, Ca$^+$ & K$^+$. Relatively to Na$^+$, Ca$^+$ profiles, the profile of K$^+$ is singular. While its depth distribution is inhomogeneous for stack 1 (intermediate V$_{Int-layer}$ = 3 nm), it is very low and nearly constant throughout the V$_2$O$_5$/V/V$_2$O$_5$ stacks 2 & 3 i.e. (intermediate V$_{Int-layer}$ = 7 & 12 nm). Besides, the K$^+$ profiles exhibit a net localized peak at the interface substrate-stacks 2 & 3. While such an accumulation at the substrate-multi-layered stacks interface is not understood, the constant diffusion within the multi-layered stacks up to the air- multi-layered stacks interface would likely affect the thermochromic properties if any. Indeed, considering the K$^+$ & Ca$^+$ concentrations within the stacks, this indirect doping would likely affect the thermochromic properties of the multi-layered stacks, especially the transition temperature as in the case of doping with various Materials including W, Mo, Mg. Cr, Ti, Nb,Cs, Sn, F, among others was reported within the literature[88–97].

Crystallographic properties: texture & crystallites orientations

Figure 8 reports the room temperature X-ray diffraction pattern of the 3 multilayered stacks of V$_2$O$_5$/ V /V$_2$O$_5$ onto borosilicate glass substrate within the Θ–2Θ diffraction configuration. The pattern was limited to the angular region of 25–31 Deg. Such an angular restriction is due to the fact there were no diffraction signatures below and above 25 Deg respectively. On the other hand, one can markedly distinguish the (011) main Bragg diffraction peak of the monoclinic VO$_2$ thermochromic active phase which for the bulk or non-strained VO$_2$ thin films generally is centred around $2\Theta \sim 27.85$ Deg. Nevertheless, those observed on the investigated samples are displaced toward higher values by at least ~ 1 Deg (samples 2 & 3). Such an angular shift can only be ascribed to a significant compressive strain/stress on the (011) reticular planes. The relative compression on such a set of reticular atomic planes is relatively high, of the order of $\Delta d_{011}/d_{011} \sim \Delta\Theta_{011}/\tan\Theta_{011} \approx 11$ & 17% for samples corresponding to intermediate V layer of 7 and 12 nm. On the other hand, the one corresponding to the thinnest intermediate V layer i.e. 3 nm seems to be under a far higher strain/stress in view of the larger angular shift of almost ~ 1.73 Deg. It is to be mentioned that this sample's XRD profile exhibits, rather, a rich diffraction pattern with 3 consecutive potential low intensity Bragg peaks centred approximately at the vicinity of 27.07, 28.29 and 29.90 Deg. This set of low intensity peaks may correspond to a sub-structure within the 1st sample i.e. (V$_{Intermediate-layer}$ = 3 nm), if any. To shed-light correctly on the nature of such a rich diffraction pattern, it would require, a priori, synchrotron type investigations. More accurately, grazing incidence x-rays diffraction studies[98–100]. One can point out to the absence of the Bragg diffraction peaks of pure Vanadium and V$_2$O$_5$ including the major most intense ones; V(100), $2\Theta \sim 42.172$ Deg) & single phase V$_2$O$_5$ (001), $2\Theta \sim 20.251$ Deg. As a pre-conclusion of this crystallographic investigation study, it is safe deducing on the significant strain/stress on the nanocrystals and their atomic reticular plans especially those of (011) orientation.
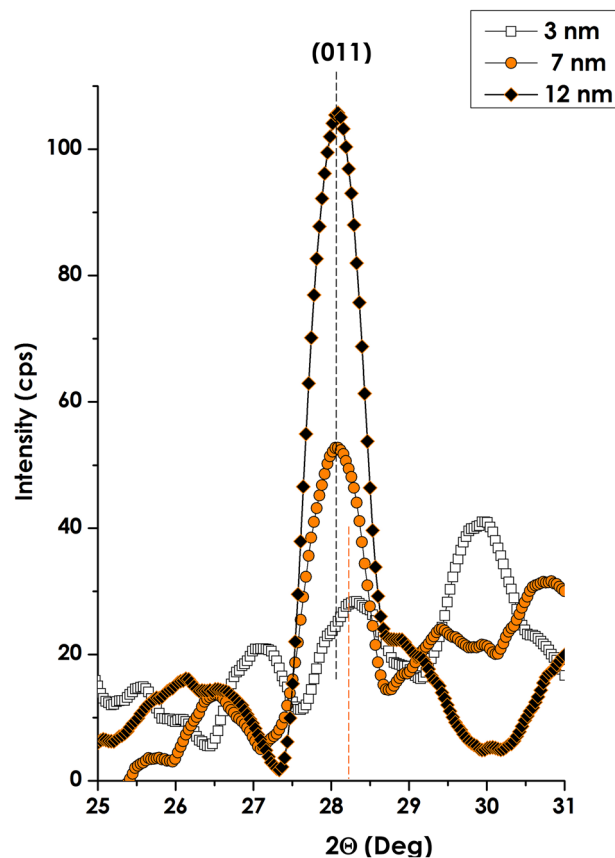
Figure 8. Crystallographic properties the various multi-layered V_2O_5(20 nm)/pure V (Variable thickness)/V_2O_5 (40 nm)deposited onto borosilicate glass substrate.

Optical properties: NIR-IR modulation tunability & control

Figure 9 reports the pivotal results of this contribution. It displays the experimental optical transmission profiles of the 3 multi-layered stacks of V_2O_5/V/V_2O_5 onto borosilicate substrate within the solar spectral range of 250–2500 nm below and above the transition temperature T_{MIT} ~ 68 °C. More precisely at 25 °C and 70 °C. Further down, they are labelled as cooling and heating respectively. As one can notice in Fig. 9a, while all of the 3 multi-layered stacks exhibit a net thermochromic signature with a crystal-clear dependence on the intermediate Vanadium layer's thickness in terms of T_{VIS} as well as the NIR-IR modulation ΔT_{TRANS}. This latter is about 1.47%, 42.01% & 32.10% for V_2O_5/3nmV/V_2O_5, V_2O_5/ 7 nm V/V_2O_5, and V_2O_5/12 nm V/V_2O_5 samples respectively. Accordingly and within this multi-layered configuration of V_2O_5/V/V_2O_5/glass substrate, it is, therefore, safe to conclude that the targeted control/tunability of the NIR-IR modulation ΔT_{TRANS} versus the intermediate V layer's thickness is validated.

Figure 9b,c display the zoom on the NIR-IR (1000–2500 nm) and VIS (250–1000 nm) solar spectral ranges. In addition to the modulation in the NIR-IR, the transmission in the VIS spectral range is also affected. The corresponding maximum of the optical transmission $\langle T_{VIS} \rangle$ is about 60.53%, 22.62% and 46.48% for V_2O_5/3 nm V/V_2O_5, V_2O_5/7 nm V/V_2O_5, V_2O_5/12 nm V/V_2O_5 samples respectively. By contrast to single VO_2 thermochromic coatings, the wavelength corresponding to the maximum of transmission in the VIS spectral range is varying with the intermediate V layer's thickness too. The spectral position of such a maximum of transmission λ^{Max}_{VIS} is centered approximately at 528.7, 682.6, and 665.1 nm for the V_2O_5/3nmV/V_2O_5, V_2O_5/7nmV/V_2O_5, V_2O_5/12 nm V/V_2O_5 samples respectively.

Figure 9d summarizes graphically Table 4 and reports on the evolution of the optical transmission in the VIS; $\langle T_{VIS} \rangle$ and the optical transmission modulation in the NIR-IR ΔT_{TRANS} ($\Delta T_{TRANS} = T_{(T \langle TMIT)} - T_{(T \rangle TMIT}$). This figure seems indicating that $\langle T_{VIS} \rangle$ and ΔT_{TRANS} variations versus the thickness of the intermediate V layer, are in opposition of phase within the considered configuration of V_2O_5/V/V_2O_5/ onto borosilicate glass substrate. This seems indicating that there is still room for optimization of ΔT_{TRANS} with a sort of trade-off between $\langle T_{VIS} \rangle$ and ΔT_{TRANS} (shaded region of Fig. 9d).

In addition to the morphological & interfacial diffusion aspects, the major findings so far identified were quantified in terms of the visible optical transmission T_{VIS} and specifically the NIR-IR optical modulation ΔT_{TRANS}.

In light of the various interfacial diffusion phenomena and the observed elevated interfacial stress/strain, it is necessary to shed-light on the effective transition temperature of the investigated multi-layered stacks and its evolution versus the intermediate Vanadium layer's thickness if any. This later, if it does should be diffusional
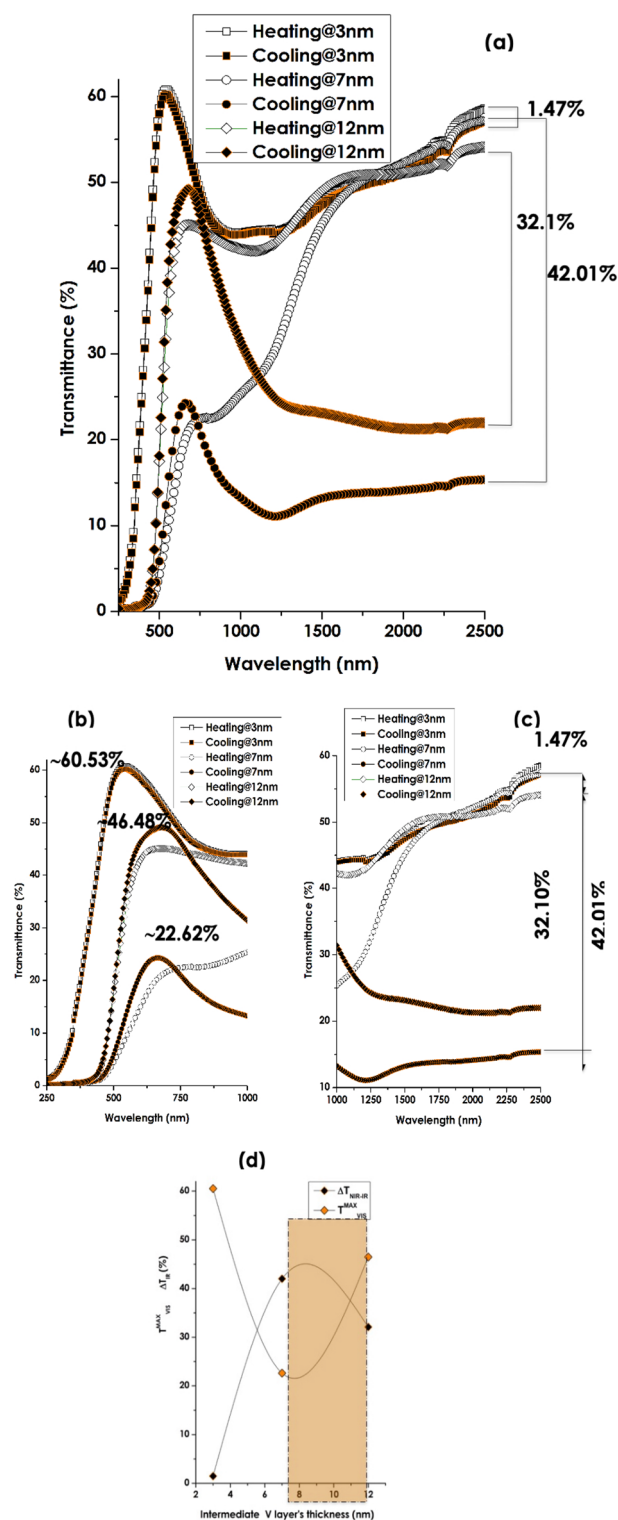
Figure 9. Optical response of the various multi-layered V_2O_5(20 nm)/pure V(Variable thickness)/V_2O_5 (40 nm) deposited onto borosilicate glass substrate. (**a**) Their room temperature XRD pattern. (**b**) Their corresponding optical transmissions at 25 °C and 70 oC within solar spectrum range of 250–2500 nm. (**c**) Their corresponding optical transmissions at 25 °C and 70 °C within NIR-IR spectral range of 1000–2500 nm and (**d**) their corresponding optical transmissions at 25 °C and 70 °C within VIS spectral range of 250–1000 nm.

Sample identification	Intermediate V layer Thickness (nm)	Maximum VIS Transmission wavelength $\langle\lambda_{VIS}\rangle$(nm)	Average VIS Transmission $\langle T_{VIS}\rangle$, (%)	Maximum Transmission T $_{(T}\langle_{TMIT}$ (%)	Minimum Transmission T $_{(T)}\rangle_{TMIT}$ (%)	Transmission Modulation (ΔT_{TRANS} (%)
1-V_2O_5/3nmV/V_2O_5	3	528.7	60.53	58.58	57.11	1.47
2-V_2O_5/7nmV/V_2O_5	7	682.6	46.48	54.02	21.92	32.1
3-V_2O_5/12nmV/V_2O_5	12	665.1	22.62	57.33	15.32	42.01

Table 4. Variation of the major optical parameters versus the intermediate V layer's thickness; Maximum VIS Transmission wavelength $\langle\lambda_{VIS}\rangle$, Maximum VIS Transmission wavelength $\langle T_{VIS}\rangle$, and the NIR-IR modulation ΔT_{TRANS} ($\Delta T_{TRANS} = T_{(T}\langle_{TMIT}) - T_{(T)}\rangle_{TMIT}$).

alkaline dopant or/and stress–strain related in view of the non-negligible large lattice mismatch between the V_2O_5 and V layers. Concerning this second aspect of crystalline lattice mismatch, this latter would likely induce a noteworthy interfacial stress/strain. This has been evidenced previously through the substantial shift of the (011) Bragg peak observed in the X-rays diffraction spectrum of Fig. 8. This interfacial stress–strain would likely affect the transition temperature of the stack as was reported in the literature by various authors[42,44,64,74]. Likewise, the observed interfacial diffusion of various alkaline ions (K^+, Na^+ & Ca^+) from the borosilicate substrate throughout the multi-layered would prospectively act as potential dopants and hence would impinge on the transition temperature. Such doping with various Materials including W, Mo, Mg. Cr, Ti, Nb, Cs, Sn, F, among others was reported within the literature[88–97]

Henceforth, hysteresis measurements were carried out on the various multi-layered stack samples as shown in Fig. 10a. This latter displays the standard hysteresis of the optical transmission versus temperature for a fixed wavelength (2500 nm) for the multi-layered stack corresponding to the intermediate Vanadium layer's thickness of 7 and 12 nm. The hysteresis for the 3 nm V was inconsequential and thus omitted. It can be noticed that the width of the hysteresis for both 7 & 12 nm V layer's thickness are almost similar in order of $\delta T \sim 7$ °C. This value is relatively smaller than the generally reported hysteresis of single VO_2 thin films which is of the order of $\delta T \geq 10$ °C. The low value of such a hysteresis ($\delta T \sim 7$ °C) might be due to the initial large density of nucleating defects during the films growth as observed and concluded by Zhang et al.[101].

To estimate the corresponding transition temperatures, the standard derivative approach is used. Figure 10b,c display the corresponding derivative hysteresis profiles. The average of the corresponding minima are 27.5 °C and 37.5 °C for the V_2O_5/V/V_2O_5 multi-layered stacks with the intermediate Vanadium layer's thickness of 7 and 12 nm respectively. This substantial lowering of the T_{MIT} which is the second prominent finding of this contribution is likely to be ascribed to the above mentioned interfacial diffusion, stress–strain and/or alkaline ions doping.

As a pre-conclusion, one might consider with provision that the investigated V_2O_5/V/V_2O_5 stacks (with 7 & 12 nm V layer's thickness) onto borosilicate glass substrate behave as an hypothetic thermochromic V_xO_y phase which exhibits a thickness dependent NIR-IR ΔT_{TRANS} with a lower phase transition temperature of $T_{MiT} = 27.5$ or 37.5 ºC while under a stern interfacial stress/strain and an alkaline doping. This conjugated doping & stress/strain effects seem to be the most plausible major parameter if one considers the extensive published literature on the subject[102–116].

Firstly, Tselev et al., and several other authors reported on the prime role of the stress/strain effects in Vanadium dioxide nanocrystals[102–106]. These studies illustrated that a complete picture of the phase transitions in single-crystalline and disordered VO_2 structures can be drawn only if both ferroelastic and metal–insulator strain effects are taken into consideration.

Secondly, similar stress/strain related behaviour was observed by Nagashima et al.[107,108]. It was found that the stress relaxation affects drastically the transport properties of strained VO_2 epitaxial thin films grown on TiO_2 (001) single crystal. When varying the film thickness ranging from 10 to 30 nm, there were no significant changes on the crystal structures. On the other hand, increasing the film thickness resulted in a drastic change on the transport properties including emerging multi-steps in the metal–insulator transition as well as an increase of the resistivity. The discrepancy between the observed crystal structure and the transport properties was related to the presence of nano-scaled line cracks due to thermal stress. It was concluded that controlling thermal stress relaxation rather than the stress due to the lattice mismatch is critical to the intrinsic nature on the transport properties of strained VO_2 epitaxial thin films.

Thirdly, and likewise, Mathevula et al.[109], reported that the interfacial stress between VO_2 thin films deposited onto highly crystalline natural substrates of mica gain considerably in crystallinity without any annealing. This unexpected crystalline growth was observed even with the drastic lattice mismatch between mica & VO_2 deposited thin films. In this later case, the VO_2-Mica substrate mismatch induced even a textured VO_2 films' crystallographic orientation with a variation of 4 orders of magnitude of the electrical resistance upon the MiT transition with a relatively small hysteresis of about $\delta T \sim 7$ °C.

Fourthly and most importantly, a similar behaviour was observed in V_2O_5 thin films by Ramana et al.[108]. In this latter case, the V_2O_5 thin films were deposited by pulsed-laser deposition and were investigated for their surface-structure evolution in relation to the growth temperature. The deposition was made onto various substrate materials and in the wide range of substrate temperatures, 30–500 °C, keeping the oxygen partial pressure at 100 mTorr. The results gave a consistent picture of the evolution of vanadium oxide film surface morphology and microstructure in terms of growth, behaviour, shape, and distribution of the grains making up films. Their grain size, surface texture, and external morphology of V_2O_5 thin films were found to be highly sensitive to the substrate temperature while the effect of substrate material characteristics is dominant only at higher temperatures. The
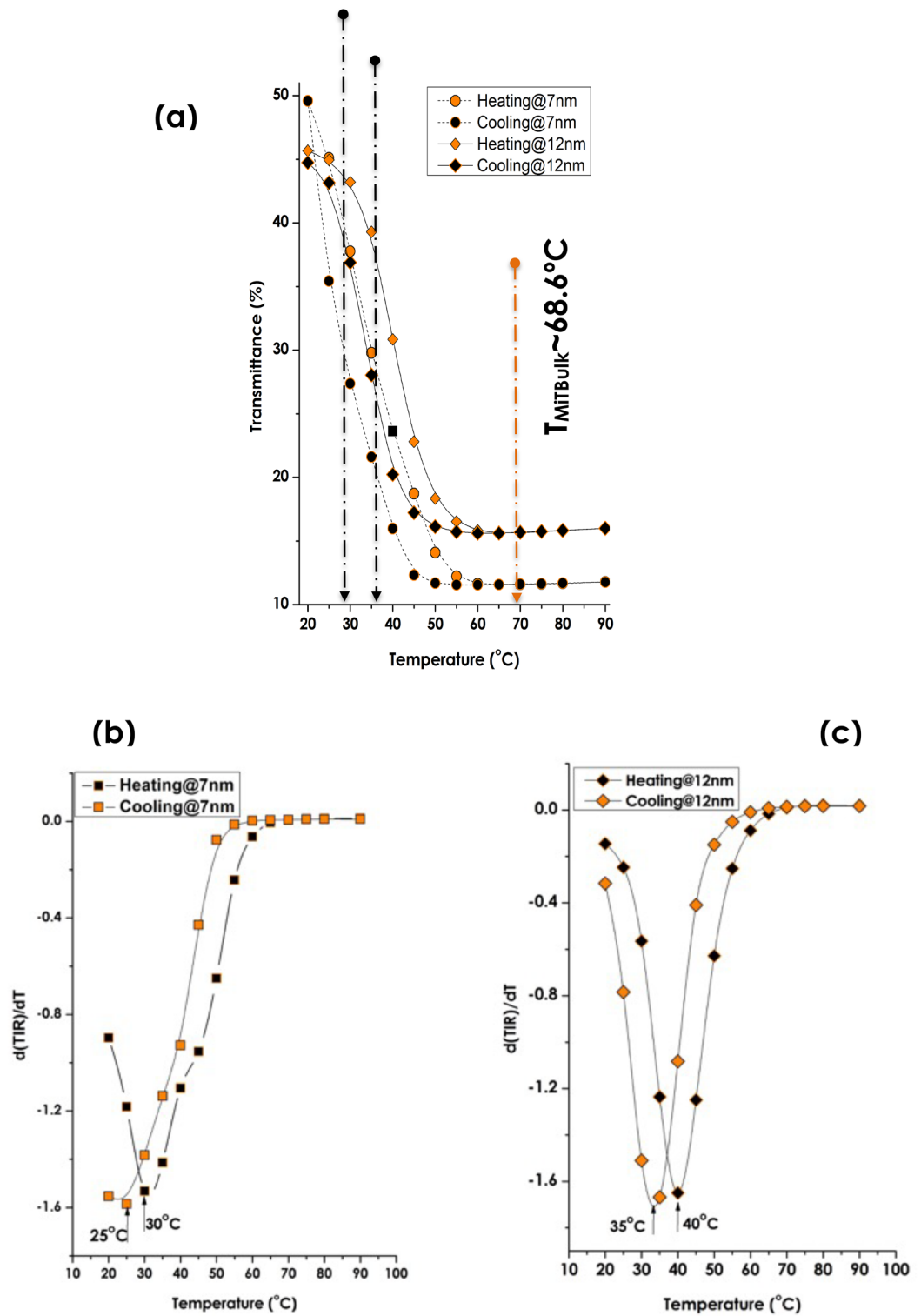
Figure 10. Thermochromic signatures & transition temperatures of the various multi-layered $V_2O_5(20\text{ nm})$/ pure V(Variable thickness)/V_2O_5 (40 nm)deposited onto borosilicate glass substrate. (**a**) Their optical transmission at 2500 nm during the cooling & heating cycles. (**b**) The derivative of the optical transmission at 2500 nm during the cooling & heating cycles of sample 2 (Intermediate V layer thickness = 7 nm). (**c**) The derivative of the optical transmission at 2500 nm during the cooling & heating cycles of sample 3 (Intermediate V layer thickness = 12 nm),

grain size varied in the range 50–600 nm and the surface roughness in the range 9–20 nm with the increasing substrate temperature for crystalline vanadium oxide thin films. Within this study, it was concluded that strain stress relaxation via thermal annealing permit the growth of highly crystalline V_2O_5 thin films.

Computational-modelling studies

As pointed out previously If one considers the O and V atomic/ionic radii, it could be, safely concluded that Oxygen is likely to diffuse from the O rich regions i.e. from layers 1 & 3 of V_2O_5 towards the O poor region i.e. towards the pure V intermediate layer. In addition to the experimental confirmation (Fig. 6), this claim can be confirmed by comparing the energy gained from forming VO_2 from bulk V and O_2 (in the gas phase) by the energy required to create a double O vacancy in the V_2O_5 lattice. The DFT simulations indicate that ~7.45 eV are gained when forming VO_2, while the energy required to create a double Oxygen vacancy in V_2O_5 is about ~5.92 eV. Therefore, the diffusion of O from V_2O_5 into the middle layer and forming VO_2 is an energetic favourable process.

To sustain or sap the stress/strain effects on the observed thermochromic properties specifically, the change in structure and electronic properties of V_2O_5 under the pressure were investigated using DFT[61]. Such studies are summarized in Figs. 11 and 12. The calculated density of states shows that the energy band gap around the Fermi level shrinks from 2.476 eV at 0 GPa and vanish at ~75 GPa. Hence, the material shows insulator behaviour characteristic at low pressure and semiconductor to metallic behaviour at higher pressures. Henceforth, one can conclude that pressure affects significantly the electronic conductivity of the V_2O_5 material at relatively excessive elevated values. These extreme pressures are exceedingly elevated to those observed in XRD of Fig. 8. Accordingly, it is safe to conclude that the observed decrease of the transition temperatures of Fig. 10 is unlikely to be interfacial strain/stress/pressure driven.
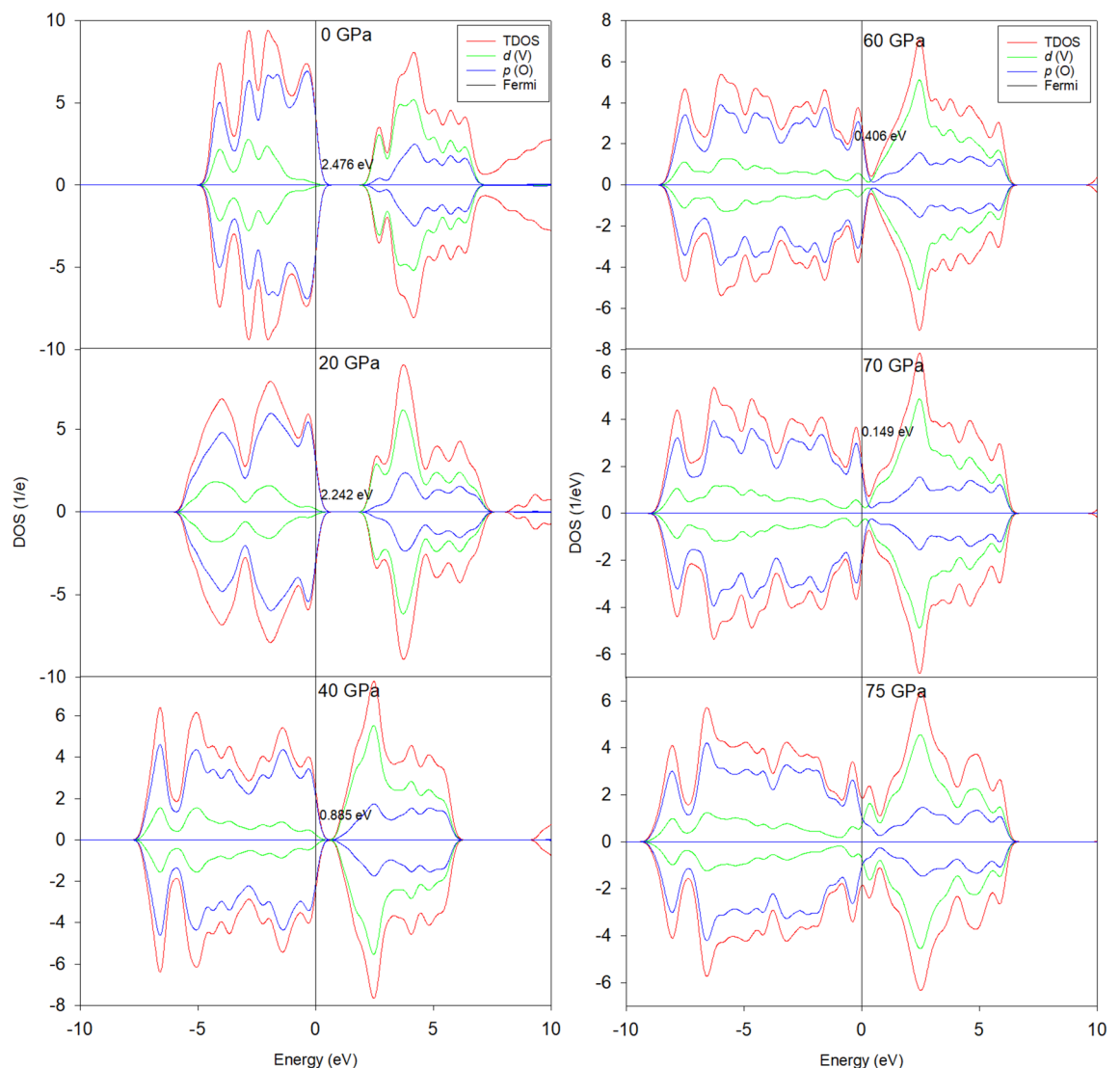

Figure 11. Total and partial density of states (DOS for V_2O_5 under pressure (20, 40, 60, 70 & 75 GPa).
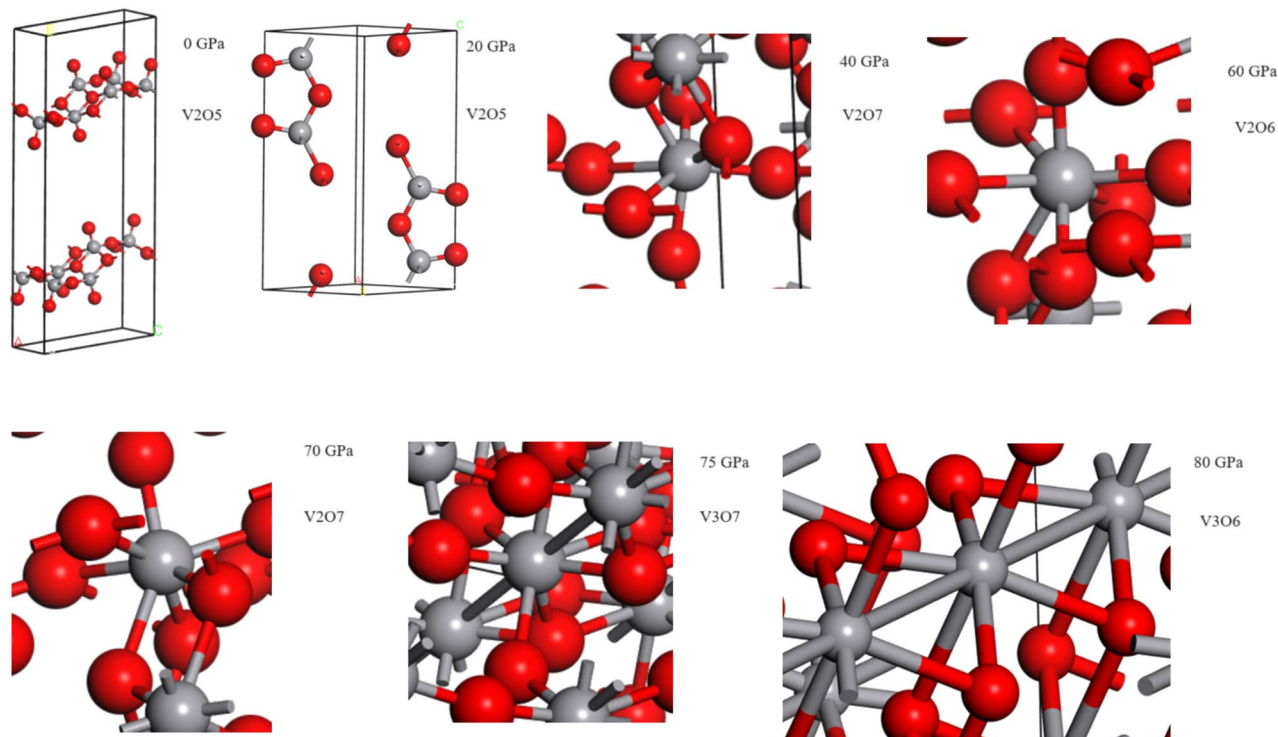
Figure 12. Structural coordination of V_2O_5 under various pressures.

In line with the SIMS observations, Na^+, Ca^{+2} & K^+ insertion into α-V_2O_5 was investigated using DFT performed in Quantum-Espresso Package[117,118] with the plane wave basis set and the PBE functional[117–119]. A plane-wave cut-off energy of 1200 eV and a Monkhorst–Pack k-mesh of $2 \times 1 \times 1$[120] was chosen for all calculations. All structures first relaxed with a convergence threshold on forces of 0.01 eV/Å. The electronic structure calculations was performed using the tetrahedron method and a finer k-mesh of $3 \times 2 \times 2$ points was utilized. For V d states, a rotationally invariant Hubbard correction was used with (U-J) = 3.5 eV[121] and also a Grimme (D2) dispersion correction with pair-wise interactions was applied on the oxygen atoms[122] to account the weak van-der Waals (vdW) interactions within the layered vanadium oxide. A single K/Na/Ca ion inserted into a $2 \times 3 \times 1$ supercell of α-V_2O_5 corresponding to a $A_{0.06}$ V_2O_5 where A is K/Na/Ca ion. Once the most favourable insertion sites with the lowest energy were identified for all ions (Fig. 13a–d), the change in electronic structure upon insertion into these preferred locations was conducted. The density of states (DOS) of pristine α-V_2O_5, K^+/V_2O_5, Na^+/V_2O_5, and Ca^{+2}/V_2O_5 are plotted displaying significant band gaps of approximately 2 eV with zero net magnetic moment. The conduction bands consist of mainly V d orbitals, while the valence band have mostly O 2p orbital contribution. It is obvious that the insertion of alkaline ions shifts the Fermi energy.

The insertion energy is calculated by subtracting the energy of V_2O_5 and metal (A) from the ionated V_2O_5, $E_{ins} = E(A/\alpha - V_2O_5) - E(\alpha - V_2O_5) - E(A)$.

The optimized structures' corresponding insertion energies for K^+, Na^+ & Ca^{+2} are -6.5, -6.8 & -13.3 eV, respectively which indicate the V_2O_5 is an effective host for ion insertion.

Since the insertion energies are relatively high, the energy barrier for intercalation of the alkaline ions into the surface of V_2O_5 using DFT was also investigated. The results are plotted in Fig. 13e, where d denote the distance from the slab in Å. Although all energies show a big barrier at around 2 Å, the intercalation energy for Na^+ ion is always negative which means that it is favorable. For K^+, if the energy required to pass the barrier at 2 Å is provided, the ion can intercalate between the layers easily. This trend indicates that the V_2O_5 is an effective host for ion insertion in general and those originating from the surface of the borosilicate substrate specifically.

As a pre-conclusion, and if one considers the intercalation aspect of Fig. 13a–d as well as the corresponding DOS distributions, one could safely conclude that the variations of the transition temperatures are likely to be caused by the alkaline ions doping and unlikely by the interfacial stress/strain. As a follow up & a foresight future investigations, the luminescence properties of the currently investigated samples will be studied[123–126]. This latter study would a priori shedlight on the role of the alkaline dopants on the local electronic & phonons configuration. Likewise, it might open new potential technological applications[127–130] in the field of luminescence.

As a pre-conclusion, and in view of both the experimental observations and the additional computational investigations, it can be safely concluded that the observed significant reduction of the transition temperature is likely to be driven by the alkaline ions doping & not the interfacial strain/stress effect.
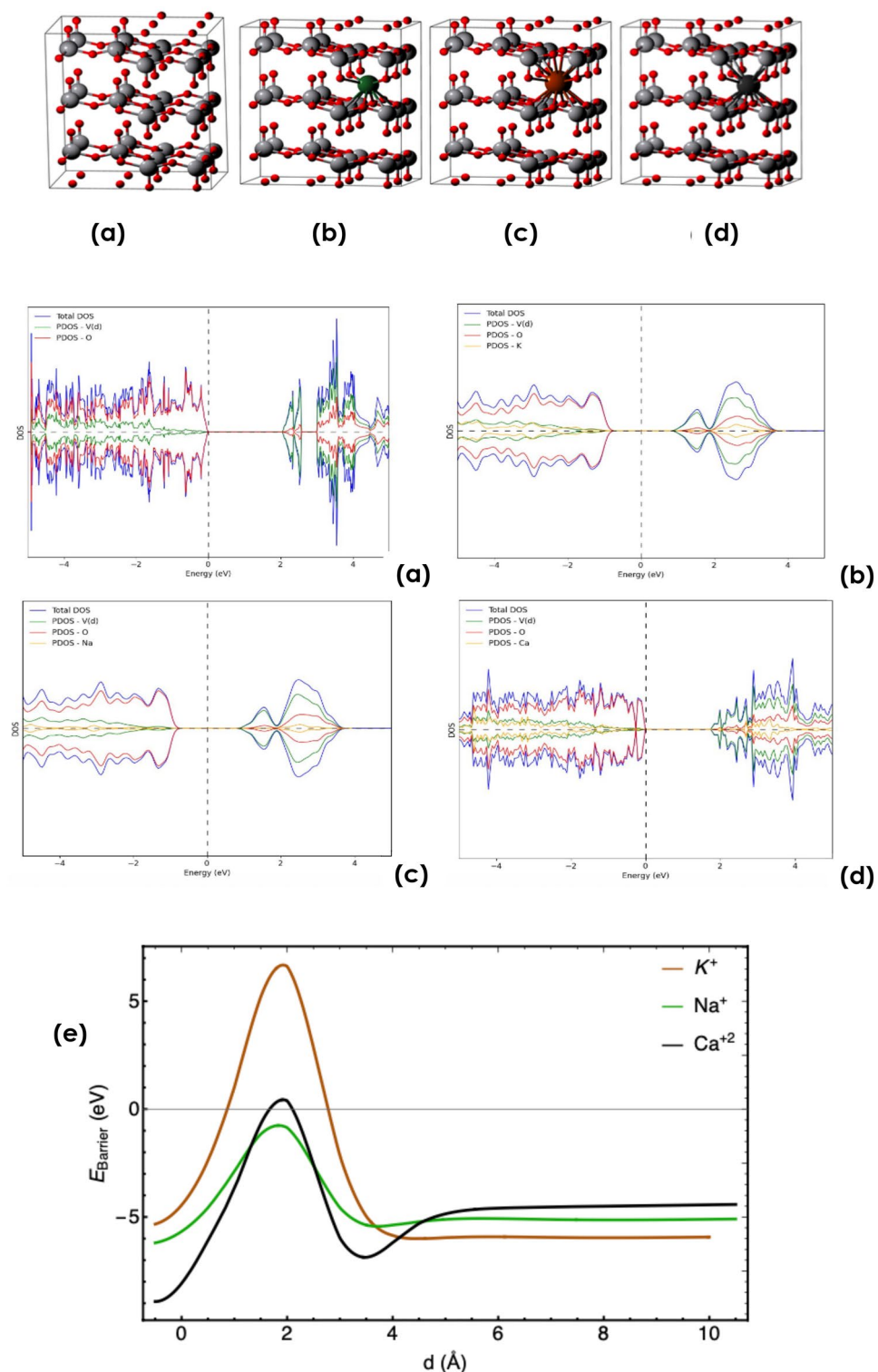
Figure 13. The optimized $2 \times 3 \times 1$ supercell of (**a**)—αV_2O_5 (**b**) Na^+/ α—V_2O_5 (**c**) K^+/ α—V_2O_5 (**d**) Ca^{+2}/ α—V_2O_5. DOS for (**a**) pristine and (**b**) K/—αV_2O_5, (**c**) Na/—αV_2O_5, & (**d**) Ca/—αV_2O_5 for the lowest-energy insertion sites. Positive and negative DOS values indicate the spin up and down, respectively. Energies are relative to the Fermi energy of each system. The partial densities of states for the different atomic species are indicated in green (vanadium), red (oxygen), and yellow (K/Na/Ca ion scaled by a factor of 100 for better visibility) in every panel, (**e**) The barrier energy for ion intercalation into the V_2O_5 slab.

Conclusion

This contribution reported on the thermochromic properties of a novel configuration consisting of $V_2O_5/V/V_2O_5$ stacks deposited onto borosilicate glass substrates by electron beam deposition. While the thickness of the V_2O_5 top and bottom layers were fixed, that of the intermediate V layer was varied within the range of 3–12 nm i.e. within the coalescence threshold of Vanadium. Such a system exhibited a crystal-clear thermochromic behaviour similar at a certain extent to that of pure VO_2 but with far lower T_{MiT} and controllable/tunable thermochromic optical modulation in the NIR-IR; ($\Delta T_{TRANS} = T_{(T\langle TMIT)} - T_{(T)TMIT}$). This latter tunability/control was validated via the intermediate V layer's thickness. In addition to an elevated interfacial diffusion, a significant stress/strain in the $V_2O_5/V/V_2O_5$ stacks was observed. In a summary, the following findings can be highlighted.

1. The investigated $V_2O_5/V/V_2O_5$ stacks onto borosilicate glass substrate exhibited a net thermo-chromic response equivalent to that of pure VO_2 thin films,
2. the investigated $V_2O_5/V/V_2O_5$ stacks onto borosilicate glass substrate exhibited a significantly low phase transition temperature of $T_{MiT} = 27.5$ & 37.5 °C,
3. Such a significant lowering of T_{MiT} is caused by Alkaline ions doping originating from the borosilicate glass substrate
4. the investigated $V_2O_5/V/V_2O_5$ stacks experience a significant interfacial diffusion especially from Oxygen rich regions to Oxygen poor regions,
5. from stoichiometric viewpoint, the investigated $V_2O_5/V/V_2O_5$ stacks seem to be equivalent to an hypothetical V_xO_y phase in between V_2O_3 & VO_2,
6. the investigated $V_2O_5/V/V_2O_5$ stacks onto borosilicate glass substrate exhibited a net controllability of the NIR-IR optical modulation ΔT_{TRANS} versus the intermediate V layer's thickness.

Data availability

The datasets used and/or analysed during the current study available from the corresponding authors on request.

References

1. Oke, T. R., Johnson, D. G., Steyn, D. G. & Watson, I. D. Simulation of surface urban heat island under 'ideal' conditions at night—Part 2: Diagnosis and causation. *Bound.-Layer Meteorol.* **56**, 339–358 (1991).
2. Santamouris, M. (ed.) *Energy and Climate in the Urban Built Environment* (James and James Science Publishers, 2001).
3. Santamouris, M. Heat island research in Europe—The State of the art. *J. Adv. Build. Energy Res.* **1**, 123–150 (2007).
4. Santamouris, A. & Synnefa, T. K. Using advanced cool materials in the urban built environment to mitigate heat islands and improve thermal comfort conditions. *Solar Energy* **85**(12), 3085–3102 (2011).
5. Papanikolaou, N. *et al.* On the impact of urban climate to the energy consumption of buildings. *Solar Energy* **70**(3), 01–216 (2001).
6. Tracking Progress: Building Envelopes. International Energy Agency (2017).
7. Ma, Y., Zhu, B. & Wu, K., Preparation and solar reflectance spectra of chameleon-type building coatings. *J. Sol. Energy* **70**, 417–422 (2001).
8. Ma, Y., Zhang, X., Zhu, B. & Wu, K., Research on reversible effects and mechanism between the energy-absorbing and energy-reflecting states of chameleon-type building coatings. *J. Sol. Energy* **72**, 511–520 (2002).
9. Karlessi, T., Santamouris, M., Apostolakis, A., Synnefa, A. & Livada, I., Development and testing of thermochromic coatings for buildings and urban structures. *Sol. Energy* **83**(4), 538–551(2009).
10. Kammen, D. M. & Sunter, D. A. City-integrated renewable energy for urban sustainability. *Science* **352**, 922–928 (2016).
11. Rogelj, J. *et al.* Energy system transformations for limiting end-of-century warming to below 1.5 °C. *Nat. Clim. Change* **5**, 519–527 (2015).
12. Granqvist, C. G. in *Handbook of Inorganic Chromogenic Materials* (Elsevier, 1995) (**and references therein (1995)**).
13. Jelle, B. P., Kalnæs, S. E. & Gao, T. Low-emissivity materials for building applications: A state-of-the-art review and future research perspectives. *Energy Build.* **96**, 329–356 (2015).
14. Morin, F. J. Oxides which show a metal-to-metal transition at the Neel temperature. *Phys. Rev. Lett.* **3**, 34 (1959).
15. Adler, D. Mechanisms for metal-nonmetal transitions in transition-metal oxides and sulfides. *Rev. Mod. Phys.* **40**, 714 (1968).
16. Wang, S. *et al.* Scalable thermochromic smart windows with passive radiative cooling regulation. *Science* **374**, 1501–1504 (2021).
17. Tang, K. *et al.* Temperature-adaptive radiative coating for all-season household thermal regulation. *Science* **374**, 1504–1509 (2021).
18. Lobastov, V.A,, Srinivasan, R., Zewail ,A.H. (2005) *Proc. Natl. Acad. Sci. USA.* **102**, 7069–7073.
19. Baum, P., Yang, D. S. & Zewail, A. H. 4-D visualization of transitional structures in phase transformations by electron diffraction. *Science* **318**(5851), 788–792. https://doi.org/10.1126/science.114772 (2007).
20. Nemraoui, O., Sella, C., Beye, A. C. & Baruch-Barak, B. Thermal induced tunability of surface plasmon resonance in Au-VO_2 nano-photonics. *Opt. Commun.* **254**(1–3), 188–195 (2005).
21. Nemraoui, O., Sella, C. & Beye, A. C. Surface plasmon resonance tunability in Au-VO2 thermochromic nano-composites. *Gold Bull.* **38**(3), 100–106 (2005).
22. Kana Kana, J. B., Ndjaka, J. M., Vignaud, G. & Gibaud, A. Thermally tunable optical constants of vanadium dioxide thin films measured by spectroscopic ellipsometry. *Opt. Commun.* **284**(3), 807–812 (2011).
23. Maaza, M. *et al.* Phase transition in a single VO_2 nano-crystal: Potential femtosecond tunable opto- electronic nano-gating. *J. Nanoparticle Res.* **16**(5), 2397 (2014).
24. Simo, A. *et al.* VO_2 nanostructures based chemiresistors for low power energy consumption hydrogen sensing. *Int. J. Hydrogen Energy* **39**(15), 8147–8157 (2014).
25. Simo, A., Kaviyarasu, K., Mwakikunga, B. & Mokwena, M. Room temperature volatile organic compound gas sensor based on vanadium oxide 1-dimension nanoparticles. *Ceram. Int.* **43**(1), 1347–1353 (2017).
26. Maaza, M. Optoelectronic ultrafast tunability in VO_2 based Mott/Peierls nanostructures. *Ann. Nanosci. Nanotechnol.* **1**(1), 1002 (2017).

27. Numan, N., Mabakachaba, B., Simo, A. & Nuru, Z. VO2-based active tunable emittance thermochromic flexible coatings. *J. Opt. Soc. Am. A Opt. Image Sci. Vision* **37**(11), 45–49 (2020).
28. Ngom, B. D., Achouri, M. & Manikandan, K. Functional nanostructured oxides. *Vacuum* **114**, 172–187 (2015).
29. Hamidi, D. *et al.* Optical limiting in pulsed laser deposited VO2 nanostructures. *Opt. Commun.* **285**(6), 1190–1193 (2012).
30. Théry, V. *et al.* Structural and electrical properties of large area epitaxial VO$_2$ films grown by electron beam evaporation. *Appl. Phys.* **121**, 055303 (2017).
31. Fisher, B., Patlagan, L. & Reisner, G. M. Sliding twin-domains in self-heated needle-like VO2 single crystals. *Sci. Rep.* **10**, 6833. https://doi.org/10.1038/s41598-020-63694-1 (2020).
32. Slusar, T. V. *et al.* Mott transition in chain structure of strained VO2 films revealed by coherent phonons. *Sci. Rep.* **7**, 16038. https://doi.org/10.1038/s41598-017-16188-6 (2017).
33. Park, J. *et al.* Measurement of a solid-state triple point at the metal–insulator transition in VO2. *Nature* **500**, 431–434. https://doi.org/10.1038/nature12425 (2013).
34. Mogunov, I. A. *et al.* Large non-thermal contribution to picosecond strain pulse generation using the photo-induced phase transition in VO$_2$. *Nat. Commun.* **11**, 1690. https://doi.org/10.1038/s41467-020-15372-z (2020).
35. O'Callahan, B. *et al.* Inhomogeneity of the ultrafast insulator-to-metal transition dynamics of VO$_2$. *Nat. Commun.* **6**, 6849. https://doi.org/10.1038/ncomms7849 (2015).
36. Xu, C. *et al.* Transient dynamics of the phase transition in VO$_2$ revealed by mega-electron-volt ultrafast electron diffraction. *Nat. Commun.* **14**, 1265. https://doi.org/10.1038/s41467-023-37000-2 (2023).
37. Matsuda, Y. H. *et al.* Magnetic-field-induced insulator–metal transition in W-doped VO$_2$ at 500 T. *Nat. Commun.* **11**, 3591. https://doi.org/10.1038/s41467-020-17416-w (2020).
38. Yoon, H. *et al.* Reversible phase modulation and hydrogen storage in multivalent VO$_2$ epitaxial thin films. *Nat. Mater.* **15**, 1113–1119. https://doi.org/10.1038/nmat4692 (2016).
39. Wu, Y. *et al.* Decoupling the lattice distortion and charge doping effects on the phase transition behavior of VO$_2$ by titanium (Ti^{4+}) doping. *Sci. Rep.* **5**, 9328. https://doi.org/10.1038/srep09328 (2015).
40. Li, G. *et al.* Photo-induced non-volatile VO$_2$ phase transition for neuromorphic ultraviolet sensors. *Nat. Commun.* **13**, 1729. https://doi.org/10.1038/s41467-022-29456-5 (2022).
41. Johnson, A. S. *et al.* Ultrafast X-ray imaging of the light-induced phase transition in VO$_2$. *Nat. Phys.* **19**, 215–220. https://doi.org/10.1038/s41567-022-01848-w (2023).
42. Wang, Y. *et al.* Reversible switching between pressure-induced amorphization and thermal-driven recrystallization in VO$_2$(B) nanosheets. *Nat. Commun.* **7**, 12214. https://doi.org/10.1038/ncomms12214 (2016).
43. Yajima, T., Nishimura, T. & Toriumi, A. Positive-bias gate-controlled metal–insulator transition in ultrathin VO$_2$ channels with TiO$_2$ gate dielectrics. *Nat. Commun.* **6**, 10104. https://doi.org/10.1038/ncomms10104 (2015).
44. Long, S. *et al.* Effects of V$_2$O$_3$ buffer layers on sputtered VO$_2$ smart windows: Improved thermochromic properties, tunable width of hysteresis loops and enhanced durability. *Appl. Surface Sci.* **441**, 764–772 (2018).
45. Leroy, J., Bessaudou, A., Cosset, F. & Crunteanu, A. Structural, electrical, and optical properties of thermochromic VO$_2$ thin films obtained by reactive electron beam evaporation. *Thin Solid Films* **520**, 4823–4825 (2012).
46. Wang, C. *et al.* New intelligent multifunctional SiO$_2$/VO$_2$ composite films with enhanced infrared light regulation performance, solar modulation capability, and superhydrophobicity. *Sci. Technol. Adv. Mater.* **18**, 563–573 (2017).
47. Chen, S. *et al.* The visible transmittance and solar modulation ability of VO$_2$ flexible foils simultaneously improved by Ti doping: An optimization and first principle study. *Phys. Chem. Chem. Phys.* **15**, 17537 (2013).
48. Pellegrino, L. *et al.* Multistate memory devices based on free-standing VO$_2$/TiO$_2$ microstructures driven by joule self-heating. *Adv. Mater.* **24**, 2929 (2012).
49. Sella, C. M., Nemraoui, O., Renard, N. & Sampeur, Y. Preparation, characterization and properties of sputtered electrochromic and thermochromic devices. *Surface Coatings Technol.* **98**(1–3), 1477–1482 (1998).
50. Kana Kana, J. B. *et al.* High substrate temperature induced anomalous phase transition temperature shift in sputtered VO$_2$ thin films. *Opt. Mater.* **32**(7), 739–742 (2010).
51. Ngom, B. D. *et al.* Competitive growth texture of pulsed laser deposited vanadium dioxide nanostructures on a glass substrate. *Acta Materialia* **65**, 32–41 (2014).
52. Ngom, B. D., Kotsedi, L. & Ghouti, M. Thermochromic VO$_2$ on Zinnwaldite Mica by pulsed laser deposition. *Appl. Surface Sci.* **314**, 476–480 (2014).
53. Madiba, I. G. *et al.* Submicronic VO$_2$-PVP composites coatings for smart windows applications and solar heat management. *Solar Energy* **107**, 758–769 (2014).
54. Granqvist, C. G. *Handbook of Inorganic Chromogenic Materials* (Elsevier, 1995) (**and references therein**).
55. Soltani, M. *et al.* Micro-optical switch device based on semiconductor-to-metallic phase transition characteristics of W-doped VO$_2$ smart coatings. *J. Vac. Sci. Technol. A* **25**, 971 (2007).
56. Soltani, M. *et al.* 1×2 optical switch devices based on semiconductor-to-metallic phase transition characteristics of VO2 smart coatings. *Meas. Sci. Technol.* **17**, 1052 (2006).
57. Leroy, J. *et al.* High-speed metal-insulator transition in vanadium dioxide films induced by an electrical pulsed voltage over nano-gap electrodes. *Appl. Phys. Lett.* **100**, 213507 (2012).
58. Numan, N. Madiba, I. G., Khanyile, B. S., Khumalo, Z. M. & Maaza, M. Hydrothermal synthesis and characterization of undoped and W-doped vanadium dioxide nanorods for thermochromic application. *J. Cryst. Growth* **590**, 126702 (2022).
59. Li, S.-Y., Niklasson, G. A. & Granqvist, C. G. Thermochromic fenestration with VO$_2$-based materials: Three challenges and how they can be met. *Thin Solid Films* **520**, 3823–3828 (2012).
60. Nagashima, K., Yanagida, T., Tanaka, H. & Kawai, T. Interface effect on the metal-insulator transition of strained vanadium dioxide ultrathin films. *J. Appl. Phys.* **101**, 026103 (2007).
61. Clark, S. J. *et al.* First principles methods using CASTEP. *Zeitschrift fuer Kristallographie* **220**, 567 (2005).
62. Jiang, M. *et al.* Improved luminance transmittance and diminished yellow color in VO$_2$ energy efficient smart thin films by Zn doping. *Ceram. Int.* **40**, 4 (2013).
63. Wu, Y. *et al.* Decoupling the lattice distortion and charge doping effects on the phase transition behavior of VO2 by titanium (Ti4+) doping. *Sci. Rep.* **5**, 9328 (2015).
64. Zhang, *et al.* VO2 thermochromic films on quartz glass substrate grown by RF plasma assisted oxide molecular beam epitaxy. *Materials* **10**, 314 (2017).
65. Lu, L. *et al.* Effect of Fe doping on thermochromic properties of VO2 films. *J. Mater. Sci. Mater. Electron.* **29**, 5501 (2018).
66. Vernardou, D. *et al.* Thermochromic amorphous VO2 coatings grown by APCVD using a single-precursor. *Solar Energy Mater. Solar Cells* **128**, 36 (2014).
67. Drosos, C. *et al.* Advancements, challenges and prospects of chemical vapour pressure at atmospheric pressure on vanadium dioxide structures. *Materials* **11**, 384 (2018).
68. Vinichenko, D. A. *et al.* Synthesis of vanadium dioxide films by a modified sol–gel process. *Inorg. Mater.* **47**, 3 (2011).
69. Pan, G. *et al.* Synthesis and thermochromic property studies on W doped VO2 films fabricated by sol–gel method. *Sci. Rep.* **7**, 6132 (2017).
70. Marvel, R. E. *et al.* Electron beam deposition of vanadium dioxide thin films. *Appl. Phys. A* **111**(3), 975–981 (2013).

71. .
72. Marvel, R. E. *et al.* Influence of deposition process and substrate on the phase transition of vanadium dioxide thin films. *Acta Materialia* **91**, 217 (2015).
73. Tan, X. *et al.* Unraveling metal-insulator transition mechanism of VO₂ triggered by Tungsten doping. *Sci. Rep.* **2**, 466. https://doi.org/10.1038/srep00466 (2012).
74. Long, S. *et al.* Effects of V₂O₃ buffer layers on sputtered VO2 smart windows: Improved thermochromic properties, tunable width of hysteresis loops and enhanced durability. *Appl. Surface Sci.* **441**, 764–772 (2018).
75. Pellegrino, L. *et al.* Multistate memory devices based on free-standing VO₂/TiO₂ microstructures driven by Joule self-heating. *Adv. Mater.* **24**, 2929 (2012).
76. Miller, M. J. & Wang, J. Multilayer ITO/VO2/TiO2 thin films for control of solar and thermal spectra. *Solar Energy Mater. Solar Cells* **154**, 88–93 (2016).
77. Zheng, J. *et al.* TiO2(R)/VO₂(M)/TiO₂(A) multilayer film as smart window: Combination of energy-saving, antifogging and self-cleaning functions. *Nano Energy* **11**, 136–145. https://doi.org/10.1016/j.nanoen.2014.09.023 (2015).
78. Zhou, L. *et al.* Modified color for VO₂/Au/VO₂ sandwich structure-based smart windows. *Appl. Phys. A* **124**, 505 (2018).
79. Han, Y.-H. *et al.* Fabrication of vanadium oxide thin film with high-temperature coefficient of resistance using V₂O₅/V/V₂O₅ multi-layers for uncooled microbolometers. *Thin Solid Films* **425**, 260–264 (2003).
80. Zhao, Y. *et al.* Simulation of smart windows in the ZnO/VO₂/ZnS sandwiched structure with improved thermochromic properties. *Energy Buildings* **66**, 545–552 (2013).
81. Khanyile, B. S. *et al.* Effect of varying the vanadium thickness layer of V2O5/V/V2O5 film on its microstructural and thermochromic properties. *J. Vacuum Sci. Technol. A Vacuum Surfaces Films* **37**(5), 051511 (2019).
82. Wang, C. *et al.* New intelligent multifunctional SiO₂/VO₂ composite films with enhanced infrared light regulation performance, solar modulation capability, and super-hydrophobicity. *Sci. Technol. Adv. Mater.* **18**, 563–573 (2017).
83. Long, S. *et al.* Thermochromic multilayer films of WO₃/VO₂/WO₃ sandwich structure with enhanced luminous transmittance and durability. *RSC Adv.* **6**, 106435 (2016).
84. Hasanuzzaman, M., Rafferty, A., Sajjia, M. & Olabi, A.-G. Properties of glass materials. *Encyclopedia Mater. Tech. Ceram. Glasses* **2**(2016), 647–657 (2016).
85. Maaza, M., Farnoux, B., Samuel, B., Sella, C. & Trocellier, P. Effect of mechanical polishing on the surface structure of glasses studied by grazing angle neutron reflectometry. *Opt. Commun.* **100**(1–4), 220–230 (1993).
86. Kumar, S. *et al.* Sodium diffusion in sodium borosilicate glass used for immobilization of high level liquid waste. *J. Radioanal. Nuclear Chem.* **274**(2), 225–228 (2007).
87. Maaza, M., Farnoux, B., Samuel, F., Sella, C. & Trocellier, P. Effect of mechanical polishing on the surface structure of glasses, studied by grazing angle neutron reflectometry. *Opt. Commun.* **100**, 220–230 (1993).
88. Lee, M. H., Kim, M. G. & Song, H. K. Thermochromism of rapid thermal annealed VO2 and Sn-doped VO2 thin films. *Thin Solid Films* **290–291**, 30–33 (1996).
89. Jin, P., Nakao, S. & Tanemura, S. "Tungsten doping into vanadium dioxide thermochromic films by high-energy ion implantation and thermal annealing. *Thin Solid Films* **324**, 151–158 (1998).
90. Paone, A. *et al.* Influence of doping in thermochromic V₁₋ₓWₓO₂ and V₁₋ₓAlₓO₂ thin films: Twice improved doping efficiency in V₁₋ₓWₓO₂. *J. Alloys Compd.* **621**, 206–211 (2015).
91. Song, L. *et al.* Preparation and thermochromic properties of Ce-doped VO2 films. *Mater. Res. Bull.* **48**, 2268–2271 (2013).
92. Kiri, P., Warwick, M. E. A., Ridley, I. & Binions, R. Fluorine doped vanadium dioxide thin films for smart windows. *Thin Solid Films* **520**, 1363–1366 (2011).
93. Hanlon, T. J., Coath, J. A. & Richardson, M. A. Molybdenum-doped vanadium dioxide coatings on glass produced by the aqueous sol-gel method. *Thin Solid Films* **436**, 269–272 (2003).
94. Chae, B. G., Kim, H. T. & Yun, S. J. Characteristics of W- and Ti-doped Vo2 thin films prepared by sol-gel method. *Electrochem. Solid State* **11**(6), D53–D55 (2008).
95. Wu, X. *et al.* Enhancement of VO2 thermochromic properties by Si doping. *Surf. Coat. Technol.* **276**, 248–253 (2015).
96. Kakiuchida, H., Jin, P. & Tazawa, M. Optical characterization of vanadium–titanium oxide films. *Thin Solid Films* **516**, 4563–4567 (2008).
97. Burkhardt, W. *et al.* Tungsten and fluorine co-doping of VO2 films. *Thin Solid Films* **402**, 226–231 (2002).
98. O. Sakata & M. Nakamura. Grazing incidence X-ray diffraction, surface science techniques (2013). Vol. 51. ISBN: 978-3-642-34242-4.
99. Shvyd'ko, Y. *et al.* Near-100% Bragg reflectivity of X-rays. *Nat. Photon* **5**, 539–542. https://doi.org/10.1038/nphoton.2011.197 (2011).
100. Paul, N. *et al.* Surface distortion of Fe dot-decorated TiO₂ nanotubular templates using time-of-flight grazing incidence small angle scattering. *Sci. Rep.* **10**, 4038. https://doi.org/10.1038/s41598-020-60899-2 (2020).
101. Zhang, H., Wu, Z., Yan, D., Xu, X. & Jiang, Y. Tunable hysteresis in metal-insulator transition of nanostructured vanadium oxide thin films deposited by reactive direct current magnetron sputtering. *Thin Solid Films* **552**, 218–224 (2014).
102. Tselev, A. *et al.* Mesoscopic metal-insulator transition at ferroelastic domain walls in VO2. *ACS Nano.* **4**(8), 4412–4419. https://doi.org/10.1021/nn1004364 (2010).
103. Tselev, A. *et al.* Symmetry relationship and strain-induced transitions between insulating M1 and M2 and metallic R phases of vanadium dioxide. *Nano Lett.* **10**(11), 4409–4416. https://doi.org/10.1021/nl1020443 (2010).
104. Wei, J., Wang, Z., Chen, W. & Cobden, D. H. New aspects of the metal-insulator transition in single-domain vanadium dioxide nanobeams. *Nat. Nanotechnol.* **4**(7), 420–424. https://doi.org/10.1038/nnano.2009.141 (2009).
105. Favaloro, T. *et al.* Direct observation of nanoscale Peltier and Joule effects at metal-insulator domain walls in vanadium dioxide nanobeams. *Nano Lett.* **14**(5), 2394–2400. https://doi.org/10.1021/nl500042x (2014) (**Epub 2014 Apr 17**).
106. Salje, E. K. H. & Kustov, S. Dynamic domain boundaries: Chemical dopants carried by moving twin walls. *Phys. Chem. Chem. Phys.* **25**(3), 1588–1601. https://doi.org/10.1039/d2cp04908b (2023).
107. Nagashima K., Yanagida T., Tanaka H., & Kawai, T. Stress relaxation effect on transport properties of strained vanadium dioxide epitaxial thin films. *Phys. Rev. B* **74**, 172106
108. Ramana, C. V., Smith, R. J., Hussain, O. M. & Julien, C. M. On the growth mechanism of pulsed-laser deposited vanadium oxide thin films. *Mater. Sci. Eng. B* **111**, 218–225 (2004).
109. Mathevula, L. *et al.* Thermochromic VO₂ on Zinnwaldite Mica by pulsed laser deposition. *Appl. Surface Sci.* **314**, 476–480 (2014).
110. Hwang, I.-H., Park, C.-I., Yeo, S., Sun, C.-J. & Han, S.-W. Decoupling the metal insulator transition and crystal field effects of VO2. *Sci. Rep.* https://doi.org/10.1038/s41598-021-82588-4 (2021).
111. Planer, J., Mittendorfer, F. & Redinger, J. First principles studies of the electronic and structural properties of the rutile VO2 (110) surface and its oxygen-rich terminations. *J. Phys. Condensed Matter.* **33**(47), 475002. https://doi.org/10.1088/1361-648X/ac2203 (2021).
112. Mohebbi, E. *et al.* Insights into first-principles characterization of the monoclinic VO₂ (B) polymorph via DFT + U calculation: Electronic, magnetic and optical properties. *Nanosc. Adv.* **4**(17), 3634–3646. https://doi.org/10.1039/D2NA00247G (2022).
113. Zhang, S., Yen Chou, J. & Lauhon, L. J. Direct correlation of structural domain formation with the metal insulator transition in a VO₂ nanobeam. *Nano Lett.* **9**(12), 4527–4532. https://doi.org/10.1021/nl9028973 (2009).

114. Tselev, A. *et al.* Interplay between ferroelastic and metal–insulator phase transitions in strained Quasi-two-dimensional VO_2 nanoplatelets. *Nano Lett.* **10**(6), 2003–2011. https://doi.org/10.1021/nl1008794 (2010).

115. Strelcov, E., Davydov, A. V., Lanke, U., Watts, C. & Kolmakov, A. In situ monitoring of the growth, intermediate phase transformations and templating of single crystal VO2 nanowires and nanoplatelets. *ACS Nano* **5**(4), 3373–3384. https://doi.org/10.1021/nn2007089 (2011).

116. Zhang, S., Kim, I. S. & Lauhon, L. J. Stoichiometry Engineering of Monoclinic to Rutile phase transition in suspended single crystalline Vanadium Dioxide nanobeams. *Nano Lett.* **11**(4), 1443–1447. https://doi.org/10.1021/nl103925m (2011).

117. Scandolo, S. *et al.* First-principles codes for computational crystallography in the Quantum-ESPRESSO package. *Zeitschrift für Kristallographie Crystalline Mater.* **220**, 574–579 (2005).

118. Perdew, J. P., Burke, K. & Ernzerhof, M. Generalized gradient approximation made simple. *Phys. Rev. Lett.* **77**, 3865–3868 (1996).

119. Dudarev, S. L., Botton, G. A., Savrasov, S. Y., Humphreys, C. J. & Sutton, A. P. *Phys. Rev. B Condens. Matter* **57**(3), 1505–1509 (1998).

120. Clark, S. J. *et al.* First principles methods using CASTEP. *Zeitschrift fuer Kristallographie* **220**(5–6), 567–570 (2005).

121. Monkhorst, H. J. & Pack, J. D. Special points for Brillouin-Zone integrations. *Phys. Rev. B* **13**, 5188 (1976).

122. Grimme, S. Semiempirical GGA-type density functional constructed with a long-range dispersion correction. *J. Comput. Chem.* **27**(15), 1787–1799 (2006).

123. Sreehari Sastry, S. & Rao, V. Structural and optical properties of vanadium doped akaline earth lead zinc phosphate glasses. *Indian J. Pure Appl. Phys.* **52**(7), 491–498 (2014).

124. Kawabe, Y., Yamanaka, A., Horiuchi, H., Takashima, H. & Hanamura, E. Luminescence of color centers formed in alkali-earth-doped yttrium orthoaluminate crystals. *J. Luminescence* **121**(2), 517–526 (2006).

125. Krasnikov, A., Mihokova, E., Nikl, M., Zazubovich, S. & Zhydachevskyy, Y. Luminescence spectroscopy and origin of luminescence centers in Bi-doped materials. *Crystals* **10**(3), 208 (2020).

126. Said, D. *et al.* Influence of vanadium in sensitized luminescence mechanism and Judd-Ofelt analysis in doped mixed ionic-electronic glass system. *Opt. Mater.* **143**, 114169 (2023).

127. Khalid Hossain, M., Shahadat Hossain, S., Hafez Ahmed, M., Ishak Khan, H. N. & Raihan, G. A review on optical applications, prospects, and challenges of rare-earth oxides. *ACS Appl. Electron. Mater.* **9**, 3715–3746 (2021).

128. Khalid Hossain, M. *et al.* Current applications and future potential of rare earth oxides in sustainable nuclear, radiation, and energy devices: A review. *ACS Appl. Electron. Mater.* **4**(7), 3327–3353 (2022).

129. Khalid Hossain, M. *et al.* A review on recent applications and future prospects of rare earth oxides in corrosion and thermal barrier coatings, catalysts, tribological, and environmental sectors. *Ceram. Int.* **48**(22), 32588–32612 (2022).

130. Munjer, M. A., Hasan, Z., Khalid Hossain, M. & Ferdous Rahman, M. The obstruction and advancement in sustainable energy sector to achieve SDG in Bangladesh. *Sustainability* **15**(5), 3913 (2023).

Acknowledgements

Author contributions

B.S.K.: Deposition & various characterizations, N.N.:various characterizations, A.S.: Theory, M.N.: AFM investigations,C.B.M.: Rutherford Backscattering investigations, Z.K.: Elastic Recoil Detection investigations, I.G.M. Deposition, B.M.: Optical characterization, H.S.: SIMS investigations, E.C.H.: Auger investigations, M.M.D.: SIMS investigations, E.L.: Auger investigations, M.H.: Interpretation & manuscript reading, A.G.: Guidance , M.C.: Guidance, P.R.: Computation & Modelling,N.L..: Computation & Modelling,R.M.: Computation & Modelling,M.A.: Computation & Modelling, M.M.: Conceptualization, interpretation & manuscript writing.

Competing interests

The authors declare no competing interests.

Additional information

Correspondence and requests for materials should be addressed to B.S.K. or M.M.

Reprints and permissions information is available at www.nature.com/reprints.

Publisher's note Springer Nature remains neutral with regard to jurisdictional claims in published maps and institutional affiliations.